

Spectral analysis of four ‘hypervariable’ AGN: a micro-needle in the haystack?

A. Bruce,¹[★] A. Lawrence,¹ C. MacLeod,² M. Elvis,² M. J. Ward,³ J. S. Collinson,³ S. Gezari,⁴ P. J. Marshall,⁵ M. C. Lam,¹ R. Kotak,⁶ C. Inserra,⁶ J. Polshaw,⁶ N. Kaiser,⁷ R.-P. Kudritzki,⁷ E. A. Magnier⁷ and C. Waters⁷

¹*Institute for Astronomy, SUPA (Scottish Universities Physics Alliance), University of Edinburgh, Royal Observatory, Blackford Hill, EH9 3HJ, U*

²*Harvard-Smithsonian Center for Astrophysics, 60 Garden St., Cambridge, MA 02138, USA*

³*Department of Physics, University of Durham, South Road, Durham, DH1 3LE, UK*

⁴*Department of Astronomy, University of Maryland, College Park, MD 20742-2421, USA*

⁵*Kavli Institute for Particle Astrophysics and Cosmology, P.O. Box 20450, MS 29, Stanford, CA 94309, USA*

⁶*Astrophysics Research Centre, School of Mathematics and Physics, Queens University Belfast, Belfast BT7 1NN, UK*

⁷*Institute for Astronomy, University of Hawaii, 2680 Woodlawn Drive, Honolulu HI 96822*

Accepted XXX. Received YYY; in original form ZZZ

ABSTRACT

We analyze four extreme AGN transients to explore the possibility that they are caused by rare, high-amplitude microlensing events. These previously unknown type-I AGN are located in the redshift range 0.6–1.1 and show changes of > 1.5 magnitudes in the g-band on a timescale of \sim years. Multi-epoch optical spectroscopy, from the William Herschel Telescope, shows clear differential variability in the broad line fluxes with respect to the continuum changes and also evolution in the line profiles. In two cases a simple point-source, point-lens microlensing model provides an excellent match to the long-term variability seen in these objects. For both models the parameter constraints are consistent with the microlensing being due to an intervening stellar mass object but as yet there is no confirmation of the presence of an intervening galaxy. The models predict a peak amplification of 10.3/13.5 and an Einstein timescale of 7.5/10.8 years respectively. In one case the data also allow constraints on the size of the CIII] emitting region, with some simplifying assumptions, to be ~ 1.0 –6.5 light-days and a lower limit on the size of the MgII emitting region to be > 9 light-days (half-light radii). This CIII] radius is perhaps surprisingly small. In the remaining two objects there is spectroscopic evidence for an intervening absorber but the extra structure seen in the lightcurves requires a more complex lensing scenario to adequately explain.

Key words: galaxies:active – galaxies:nuclei – gravitational lensing: micro – accretion, accretion discs – quasars: absorption lines – quasars:emission lines

1 INTRODUCTION

The identification of a class of AGN transients that are smoothly evolving, by factors of several, on year-long timescales (Lawrence 2012; Lawrence et al. 2016, hereafter L16) has raised a number of interesting questions regarding the underlying cause. These ‘hypervariable’ AGN may simply be at the extreme end of the tail of typical AGN variability (MacLeod et al. 2010, 2012) or, perhaps more interestingly, there may be an extrinsic cause. Plausible mechanisms for these transients include: accretion events/instabilities;

tidal disruption events (TDEs) or extinction events. A fourth possibility, and the focus for this particular work, is that some of these AGN transients are actually rare, high amplitude microlensing events. If this is the case, through analysis of multi-epoch spectroscopy and simple lensing models, we have the potential to uncover valuable information on the inner-most regions of these enigmatic objects.

Observational studies of the microlensing seen in multiply-imaged AGN are well established and provide the means with which one can ascertain properties intrinsic to those objects (Irwin et al. 1989; Eigenbrod et al. 2008; Morgan et al. 2010; Blackburne et al. 2011; Mosquera & Kochanek 2011; Sluse et al. 2012;

[★] E-mail: alb@roe.ac.uk

(Jiménez-Vicente et al. 2012, 2014; MacLeod et al. 2015). This involves a monitoring of the AGN components in order to ascertain both the level of variability intrinsic to the AGN and that due to microlensing, typically a low-level ‘flickering’, in one or more of these components. In contrast, the AGN in this paper exhibit no clear sign of strong lensing effects and are varying significantly and smoothly (relative to typical AGN behaviour). If a rare, high amplitude microlensing event is the cause of this variability, this places these previously unknown AGN in a different regime to their multiply imaged counterparts.

In this paper, four promising AGN transients are selected as candidates for an exploration of the microlensing scenario and its consequences. That is, the hypothesis that an intervening stellar-mass object is responsible for the bulk variability seen in these objects. It should be noted that microlensing events will not explain all hypervariable AGN activity, rather they likely describe a subset of this interesting population. In the interest of brevity this paper will focus entirely on the microlensing scenario but interested readers should refer to L16 and references therein for more discussion on the alternative variability scenarios.

Section 2 describes our sample selection, observational data and reduction pipeline. Spectroscopic results are detailed in Section 3. Section 4 outlines the procedures used for exploring different lensing models with results detailed in Section 5. In Section 6, the implications for future work and the advantages/disadvantages over existing microlensing studies involving multiply-imaged AGN are discussed. Cosmological calculations in this paper make use of Planck13 values (Planck Collaboration et al. (2014); $H_0 = 67.8$, $\Omega_\Lambda = 0.693$).

2 OBSERVATIONS

2.1 Target selection

2.1.1 Parent sample

The four objects in this paper are selected from a larger sample of highly variable AGN, discovered as part of a wider transient search initially designed to look for tidal disruption events (TDEs) around quiescent black holes. A significant fraction of candidate events varied on longer timescales than that expected for TDEs or supernovae and were subsequently revealed to be AGN. The transients were identified by looking for changes of greater than 1.5 magnitudes in the Pan-STARRS 1 3π Steradian Survey data when compared with the SDSS footprint from around a decade earlier. In addition, the transient had to be located within $0.5''$ of an object classified as a ‘galaxy’ in the DR7 catalogue. Approximately two-thirds of the flagged objects have been spectroscopically confirmed as type-I AGN and it is these which make up the larger ‘hypervariable’ AGN sample, currently 63 objects. For further details see L16.

2.1.2 Selection criteria for this paper

To explore the microlensing hypothesis, objects were selected from the hypervariable AGN sample based on the following criteria: First, that the photometry displays signs of smooth evolution on long timescales with a change in

Table 1. Summary of the target selection criteria noted in Section 2.1.2

short ID	SDSS ID	single-peak?	double-peak?	int-gal?
J084305	J084305.54+550351.3	yes	no	no
J094511	J094511.08+174544.7	yes	no	no
J142232	J103837.08+021119.6	no	yes	yes
J103837	J142232.45+014026.8	no	no	yes

magnitude of $\Delta g > 0.5$ mag over the period of spectral observations. Second, that there are a minimum of two spectral observations separated by at least one year (observed frame). The former favours microlensing events over intrinsic variability and the latter increases the chance of observing spectroscopic trends, allowing further testing of the microlensing hypothesis.

Additional factors which favour a microlensing scenario are summarised in Table 1. Here, the presence of a near-symmetric single peak or double-peaked structure in the lightcurve, or evidence for an intervening galaxy, and hence lens repository, are noted. At least one of these additional factors was required in the target selection process leaving a total of four microlensing candidates for consideration. Any evidence for an intervening galaxy will be discussed as part of the spectroscopic results for that target (Section 3).

2.2 Photometry

2.2.1 SDSS data

SDSS data used in this paper are DR9 (Ahn et al. 2012) *cmodel* g-band magnitudes. These should provide the most reliable magnitude estimate for an extended object in a single band and should also agree with the PSF magnitudes for stars. Not all bands are best-fit with extended models for these objects, as might be expected with the presence of an AGN component. Also, from DR7 to DR9, J103837 has had the classification changed to stellar. The least reliable data is that for J142232 which, in addition to being faint, is flagged as having been affected by a cosmic ray hit.

2.2.2 Pan-STARRS data

The Pan-STARRS 1 3π g_{p1} data used in this paper are from the PV1.2 data release (Schlafly et al. 2012; Tonry et al. 2012; Magnier et al. 2013) and magnitudes have been calculated from the PSF fluxes and associated zero-points.

2.2.3 Liverpool Telescope data

The Liverpool Telescope (LT) provides finer sampling of each transient in the AGN sample and was also instrumental in the classification of the Pan-STARRS transients. The LT is a fully robotic 2.0m telescope situated on La Palma and operated by Liverpool John Moore’s University (Steele et al. 2004). The transients were initially monitored every few days in u_{LT} , g_{LT} and r_{LT} to determine how fast they were evolving and then roughly every few weeks. Scheduling and weather constraints sometimes meant that there was not always the desired cadence on some targets. The observing programme

with the LT is still ongoing. Only the g_{LT} data is utilised in this paper.

2.2.4 CRTS data

In addition to the SDSS and LT photometry, there are data from the the Catalina Real-Time Transient Survey (CRTS) (Drake et al. 2009). This survey makes use of three different telescopes and allows us to recover pre-Pan-STARRS era lightcurves for some of the objects. A note of caution is that this survey uses clear filters calibrated to a V-band zero-point so colour effects may be significant. An approximate magnitude offset has been applied so that the lightcurve appears consistent with the other data sets for each target and the data have also been seasonally averaged for clarity. Due to the the uncertainty regarding colour effects, the CRTS data is not used in the modelling process.

2.2.5 Filter approximation

For the purposes of this paper, we assume that the differences between the g_{SDSS} , g_{PI} and g_{LT} filters can be neglected and designate magnitudes as simply g . This should be reasonable given that we expect the photometric uncertainty to be dominated by intrinsic AGN variability, typically 0.1 mag or greater. For the microlensing models, magnitude to flux conversions are performed assuming an effective wavelength of 4770Å.

2.3 Spectroscopy

2.3.1 WHT data

The majority of the spectral observations were performed on the 4.2m William Herschel Telescope (WHT), La Palma, using the ISIS long-slit spectrograph. The 5300 dichroic was used along with the R158B/R300B grating in the red/blue arms respectively, along with the GG495 order sorting filter in the red arm. Typically 2× binning in the spatial direction was used to improve the signal to noise ratio along with a narrow CCD window to reduce disk usage and readout times. This setup gives a spectral resolution of $R \sim 1500$ at 5200Å in the blue and $R \sim 1000$ at 7200Å in the red for a slit width of 1" and total coverage $\sim 3100\text{--}10600\text{Å}$.

Typically calibration images were taken at the start of each night including bias frames, lamp flats and CuNe/Ar arc lamp images. Spectroscopic standard stars were imaged at $\sim 2\text{hr}$ intervals throughout the night though this cadence was not always possible. Observations were carried out at the parallactic angle and further observational details for each target in this paper are given in Table 2. Exposures were taken in 1800s increments and the number of shots on target was adjusted based on the latest g_{LT} photometry.

2.3.2 MMT data

A small number of observations were made with the blue arm spectrograph on the 6.5m MMT situated on Mount Hopkins, Arizona. Here, the 300 g/mm grating was used with 2× binning in the spatial direction. A filter wheel issue meant that no order-sorting filter was used. This may affect the third epoch for target J094511 and fourth epoch for J084305. Due

to variable conditions and a nearby bright Moon, the 6th epoch for J142232 was very poor and will not be used in the analysis.

2.3.3 Spectroscopic Reduction pipeline

A reduction pipeline was created using custom PyRAF scripts and standard techniques. After bias-subtraction and flat-fielding the cosmic rays were removed using the LACOS_SPEC script (van Dokkum 2001). The spectra were then extracted and wavelength calibrated using the arcs obtained that night. In order to minimise problems with the calibration due to temperature variations or instrument flexure an additional step was to offset each red/blue spectrum by a small amount, typically $\sim \pm 0\text{--}3\text{Å}$ to ensure the prominent atmospheric oxygen line at 5577.338Å had the correct wavelength in all observations. Flux calibration was performed using a single standard star and the mean extinction curve for the observatory. Where target observations were bracketed by standard star observations, the one least affected by transparency issues was used, i.e. the standard with the superior `sensfunc` response. To better enable the combination of the red and blue data the inner wing of each spectrum, where the response of the instrument declines steeply, was flux calibrated separately. The final step was to average all calibrated spectra and rebin to a linear wavelength scale.

Long-slit spectroscopy can suffer from transparency problems which affect the absolute flux calibration. In order to minimise these effects, each target spectrum has been rescaled. For three of the targets a smooth interpolation through the LT photometry was used to correct the spectra. In the case of J084305 and J094511, this was done by rescaling to the working microlensing model. For J142232, this was accomplished using a cubic-spline fit to the LT lightcurve. The fourth target, J103837, does not produce a satisfactory cubic-spline fit at all epochs due to a poorer LT cadence. Instead, the spectra for this target have been re-scaled so that the measured $[\text{OIII}]_{5007}$ flux, tied to the third epoch, remains constant. This method will suffer if there are significant seeing changes and it may even be possible that on these year-long timescales there will be some intrinsic narrow line variability (Peterson et al. 2013). Spectral fluxes were measured using an LT g-band transmission curve¹. The scaling factors applied are noted in Table A1.

2.3.4 Spectral fitting

For the spectral fitting process a Python package, `lmfit`, was used. This is a non-linear optimization and curve fitting tool that builds on a Levenberg-Marquardt algorithm. It was used to fit a single gaussian component to the emission lines and provide a power-law fit to approximate the local continuum. The power law used in the fitting routine takes the form

$$F_{\lambda} = A(\lambda/5100\text{Å})^{\beta} \quad (1)$$

where A is the normalisation and β is the power-law slope. In addition to the above components, a template fit was used to

¹ <http://telescope.livjm.ac.uk/TelInst/Inst/IOO/>

Table 2. Details of the spectral observations carried out for the objects listed in this paper. The airmass values reflect the mean airmass over the duration of the observation(s). Magnitudes estimates are approximations based on the LT photometry. Seeing estimates reflect the range in measured FWHM of the central region of the blue arm trace for each image.

target	scope	date	exposures	g_{mag}	slit	seeing	airmass	notes
J084305-1	WHT	20130209	1 × 1800s	20.0	2''	2.2''	1.74	dark, patchy cloud, variable seeing
-2	WHT	20130331	2 × 1800s	20.2	1''	1.1-1.2''	1.12-1.14	Moon 73%(sep 122°), stable
-3	WHT	20141217	4 × 1800s	21.1	2''	2.0-2.7''	1.51-1.24	dark, variable seeing
-4	MMT	20150310	2 × 1800s	21.3	1.5''	0.8-1.1''	1.1-1.09	Moon 82%(sep 96°), variable seeing
J094511-1	WHT	20130515	2 × 1800s	20.7	1''	1.3''	1.18-1.28	Moon 30%(sep 24°), stable
-2	WHT	20140207	4 × 1800s	21.1	1''	1.0-1.4''	1.34-1.08	Moon 63%(sep 80°), light cloud
-3	MMT	20150309	2 × 1800s	21.5	1.5''	0.8-0.9''	1.06-1.04	Moon 89%(sep 63°), variable seeing
J142232-1	WHT	20130211	2 × 1800s	20.0	1.5''	1.8-2.0''	1.24-1.18	dark, variable seeing
-2	WHT	20130515	1 × 1800s	20.1	1''	1.8''	1.34	dark, stable
-3	WHT	20130807	1 × 1800s	20.2	1''	1.1''	1.58	dark, stable
-4	WHT	20140207	2 × 1800s	20.6	1''	1.1-1.2''	1.14-1.13	dark, stable
-5	WHT	20140724	4 × 1800s	21.0	1''	1.6-2.1''	1.25-1.93	dark, stable
			1 × 900s					
(unused) -6	MMT	20150309	2 × 1800s	21.0	1''	-	1.38-1.28	Moon 89%(sep 14°), variable, v. poor
-7	WHT	20150423	4 × 1800s	21.0	1''	1.6-1.9''	1.25-1.68	dark, stable
J103837-1	WHT	20130211	1 × 1800s	19.7	1.5''	1.9''	1.13	dark, variable seeing
-2	WHT	20130515	1 × 1800s	20.2	1''	1.3''	1.38	Moon 30%(sep 40°), stable
-3	WHT	20150421	2 × 1800s	19.8	1''	0.8-0.9''	1.13-1.12	dark, stable

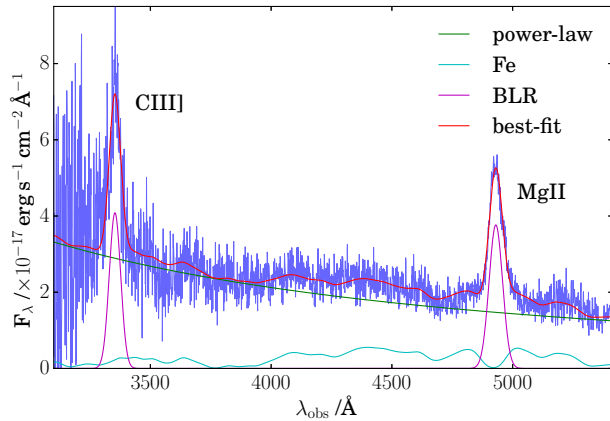


Figure 1. Example of the fitting process for target J094511. The components include: power-law (green), Gaussian line fits (magenta), convolved iron template (cyan) and overall best fit (red).

estimate the Fe contribution. In the UV, the empirical template is that from [Vestergaard & Wilkes \(2001\)](#) and in the optical, where possible, that of [Véron-Cetty et al. \(2004\)](#). The Fe template is convolved with a gaussian in order to better approximate the true blended Fe emission. The width of the convolving gaussian was set to match that of the broad MgII/H β components in the UV/optical respectively. Before performing any fits the spectra are first corrected for Milky Way extinction using the A_V values in Table 3 and the extinction law in the optical from [Cardelli et al. \(1989\)](#). No attempt has been made to correct for host galaxy reddening at this stage. The most prominent telluric features above 6860 Å were masked out during the fitting process. When fitting H β the narrow line widths and centres were tied to that of [OIII] $_{5007}$. An example fit is shown in Fig. 1.

Table 3. Information on the targets in this paper. The A_V values are those obtained from [Schlafly & Finkbeiner \(2011\)](#) assuming an R_V of 3.1.

target	RA	dec	z	A_V
J084305	08 43 05.55	+55 03 51.4	0.8955	0.0824
J094511	09 45 11.08	+17 45 44.7	0.758	0.0718
J103837	10 38 37.09	+02 11 19.7	0.620	0.0877
J142232	14 22 32.45	+01 40 26.7	1.076	0.09

3 SPECTROSCOPIC RESULTS

The results from the spectroscopic analysis are presented in three key figures. Figure 2 shows the target lightcurves and line flux evolution. The line fluxes have been plotted relative to the first epoch to allow quick comparison. Figure 3 shows the evolution of the systemic velocity offsets and emission line widths. Figure 4 shows the evolution of the spectral profiles after continuum and Fe template subtraction. For clarity, a median filter has been applied to the broad lines. Additional measurements can also be found in Table A1. The observed spectra are shown in Figures A1, A2, A3, A4.

Three of the four targets, J084305, J094511 and J142232 show clear evidence for a differential evolution of the continuum with respect to the line fluxes. In general, the continuum decreases by a factor ~ 4 and, to a lesser degree, the CIII] flux tracks this change. The MgII flux either tracks the continuum change weakly or is consistent with no change at all. The photometry indicates that the targets have been evolving smoothly over this period. A more detailed summary of each object now follows and the reader should refer back to the figures mentioned in the previous paragraph.

Any evidence for an intervening galaxy, which would lend weight to the microlensing scenario, will be presented on a per target basis.

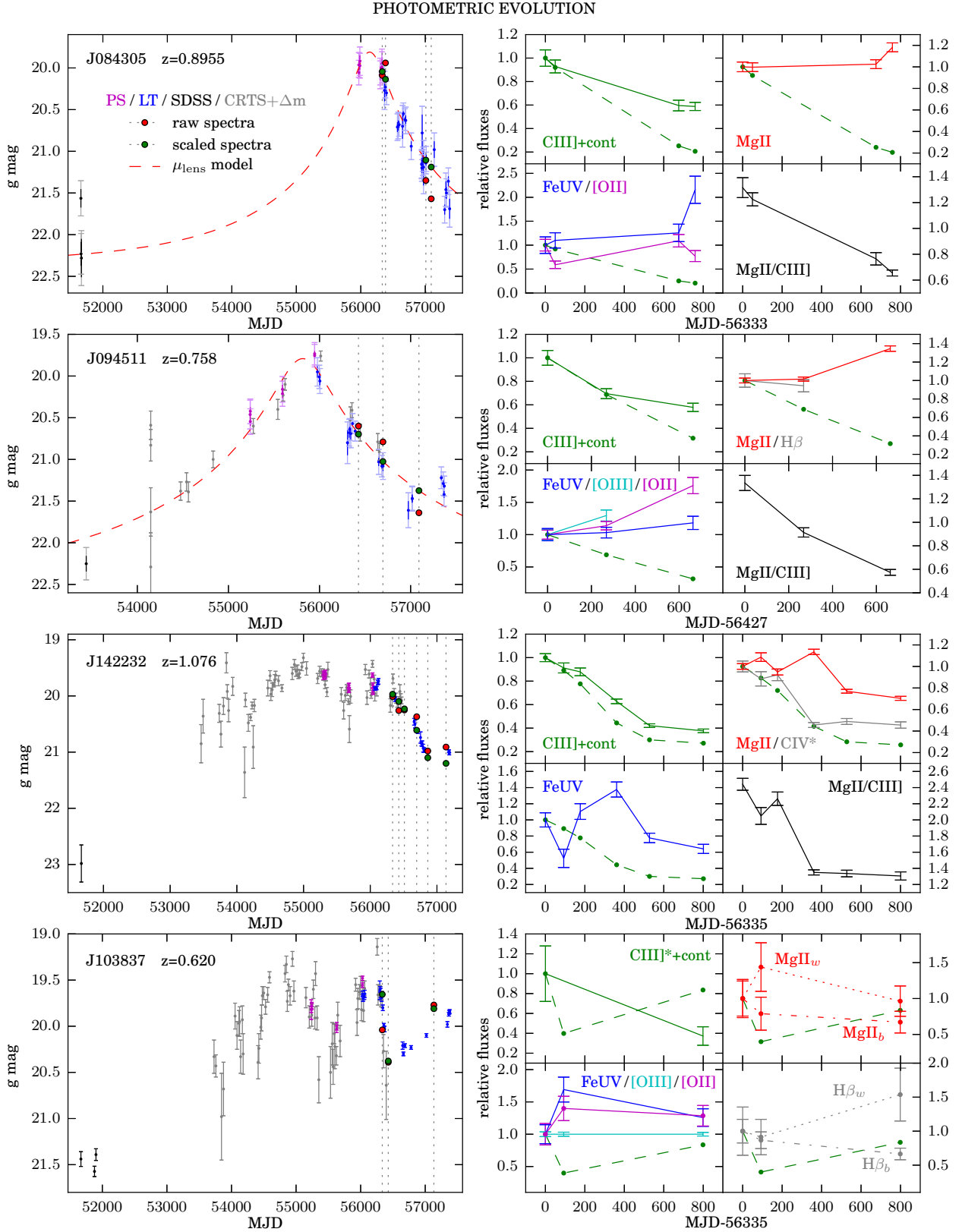


Figure 2. *Left:* Composite lightcurves for each target including spectral epochs. The red circles show the raw spectral magnitudes before rescaling as per Sec. 2.3.3 and the green circles show the rescaled values. CRTS data have offsets of +0.1/0.1/0.4/0.2 mag respectively. The extended tails on the errorbars for J084305 and J094511 reflect the errors used in the microlensing analysis. *Right:* Relative fluxes of the various measured spectral components. For the first three targets, the fourth panel shows the MgII/CIII] ratio. For J103837, the two Gaussian components used in the fit (broad and wide) are displayed. Asterisks denote less reliable values as noted in the text. The green dashed line reflects the continuum under CIII] in each case.

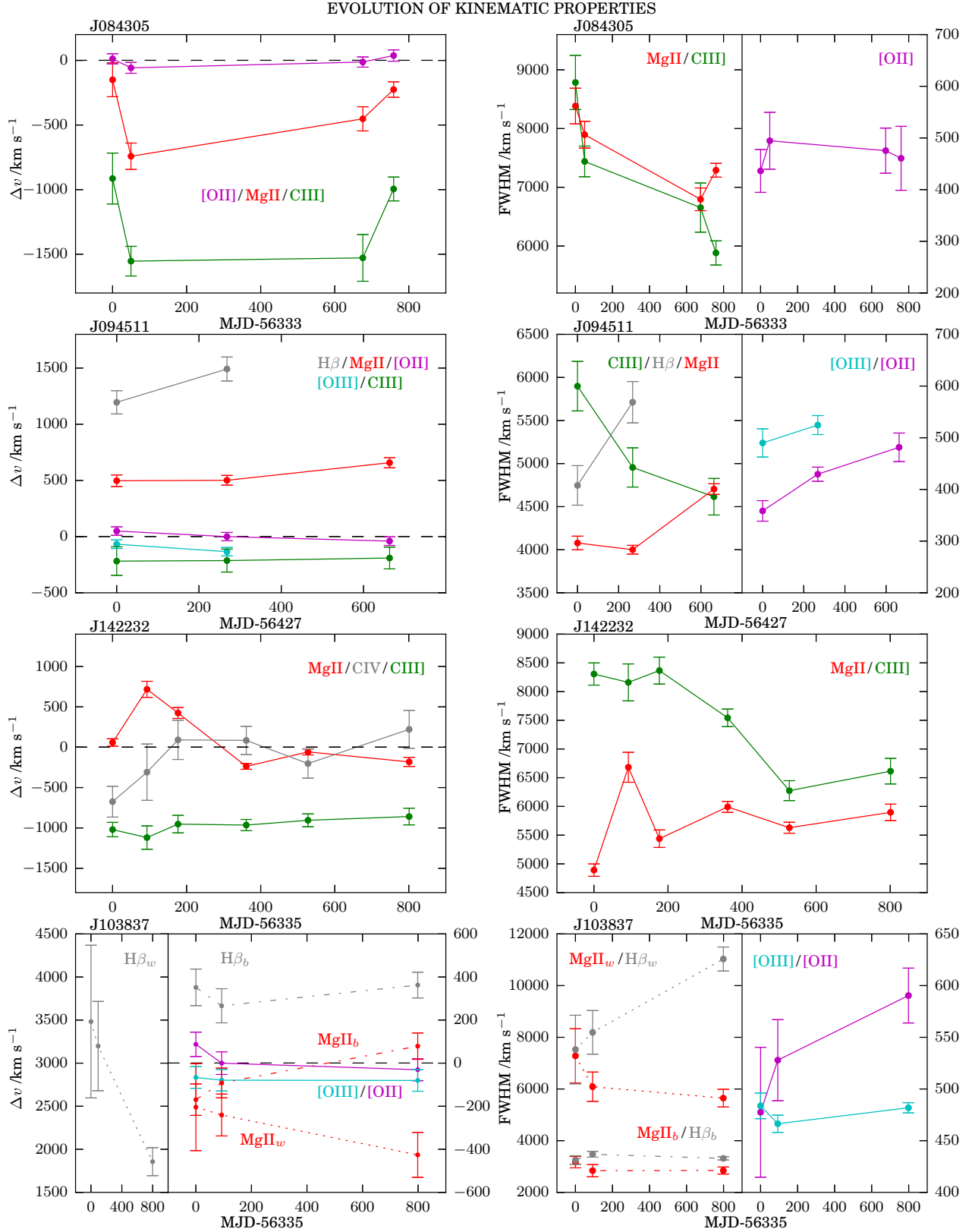


Figure 3. *Left:* Velocity offsets for the centre of the measured line profiles for each target assuming rest-frame wavelengths, in \AA of: CIV(1549); CIII](1909); MgII(2800); [OII](3727); $\text{H}\beta$ /[OIII](4861/5007). The AGN systemic redshift/velocity is determined from the median of the [OII] centres. In the case of J142232, due to a lack of observed narrow lines, MgII has been used. The error bars in this case only reflect the uncertainty in the measured line center and omit the additional systemic velocity uncertainty. The FWHM of CIV for J142232 is not shown as this value was tied to that of CIII] in the fitting process. *Right:* FWHM of the measured line profiles for each target.

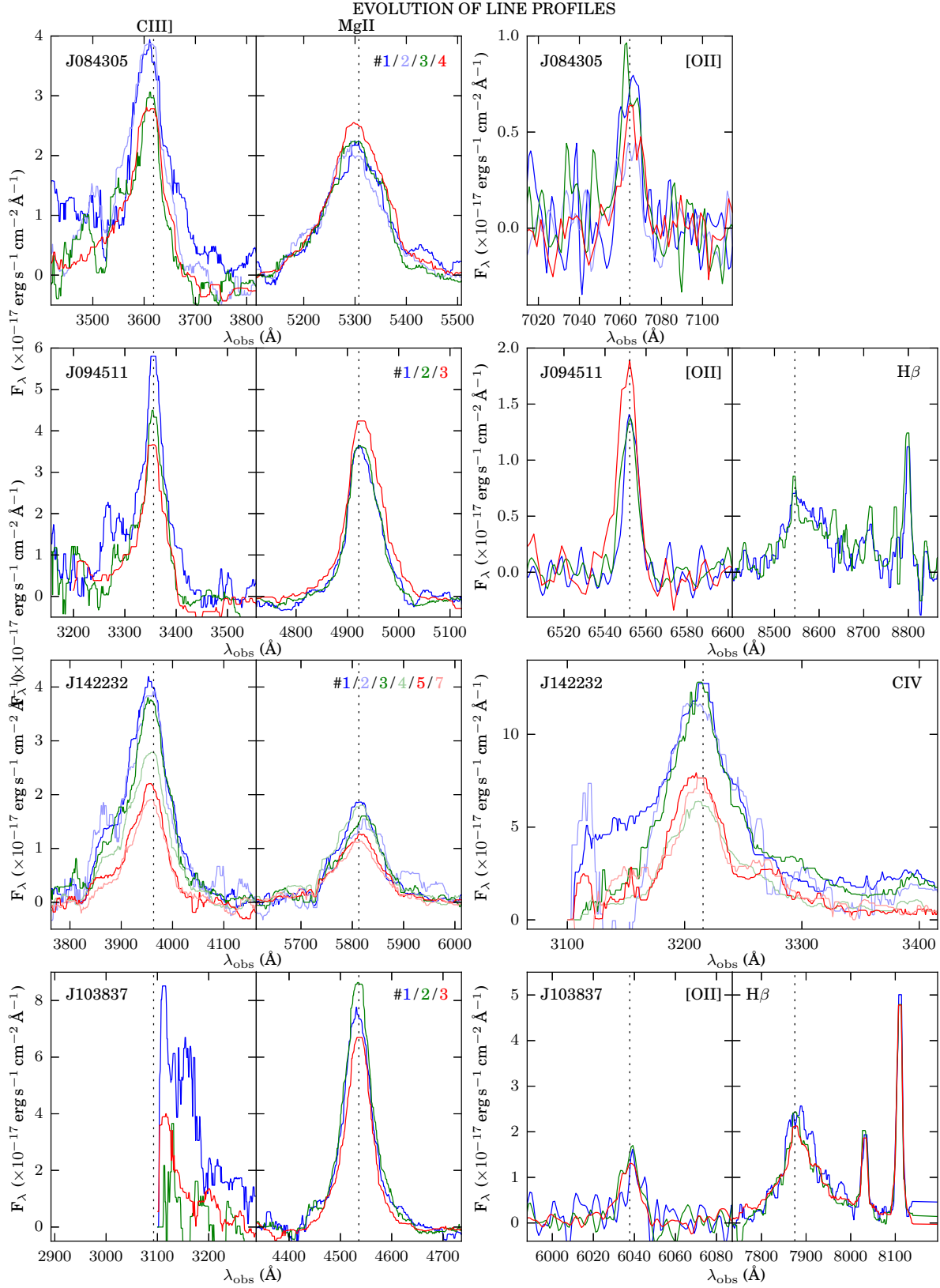


Figure 4. *Left:* CIII] and MgII profiles for each object. For J103837, the profile is truncated due to the blue arm cutoff. *Right:* Additional emission line profiles measured in the fitting process. For clarity all plots, barring those for [OII], have had a median filter applied.

3.1 J084305

The lightcurve of this target shows a smooth decline of ~ 0.6 mag/yr from a peak more than two magnitudes brighter than the SDSS observations sixteen years ago. There are no CRTS data which allow us to see the pre-Pan-STARRS evolution. There are two spectral epochs near the observed maximum around 56100 MJD and a further two after a decline of at least one magnitude. The most recent photometry suggests the target is now returning to the level of the Sloan era. Of the three SDSS epochs, two are at $g \simeq 22.25$ mag and the third has the higher value of $g = 21.56$ mag which may indicate a problem with the Sloan *cmodel* fit(s). The microlensing model shown, to which the spectra have been rescaled, does a good job of reproducing the large amplitude changes. Further details on the model are in Section 5.1.1.

As to the spectral evolution, the continuum is seen to drop by a factor of five over the period spanned by the observations. The CIII] flux shows a corresponding drop by a factor of ~ 2 . In contrast, the MgII and Fe fluxes are consistent with no change or perhaps a late increase. Both the MgII and CIII] lines get narrower during the decline. In addition, both lines are blueshifted relative to the systemic velocity, CIII] more so than MgII. There are intriguing but inconclusive signs of an evolution of the offset velocities, which shift blueward by 500 km/s or so and then recover. There are also apparent changes in the red wing of the MgII profile and both wings of CIII], most notably around the expected position of the fainter AIII component. The scatter seen in the [OII] flux may be due to slit width changes.

There are no clear spectral features suggestive of an intervening galaxy but this possibility cannot yet be ruled out. The microlensing model for this target shows that any intervening galaxy flux will be at least a factor of two below the AGN/host baseline flux in the g-band, making spectroscopic detection during an ongoing event difficult. In addition, two of the three SDSS epochs are flagged as having issues with the Petrosian radii. This may simply be due to noise or is perhaps an indicator of morphological issues.

3.2 J094511

Since the SDSS epoch some eleven years ago, this target has been evolving at around ~ 0.4 mag/yr and displays an approximately symmetric lightcurve about a peak around 56000 MJD, with an apparent dip/rise after the 57000 MJD mark. There are three spectral epochs for this object spread over two years, after the maximum, with a factor ~ 2 decrease in luminosity over this period. As with J084305, the spectra have been scaled to the microlensing model (Section 5) though the accuracy of the third epoch scaling is less certain due to the additional structure in the lightcurve at this point.

As with J084305, there is a marked difference between the evolution of MgII and CIII] fluxes. CIII] drops to $\sim 60\%$ of the initial value while MgII is consistent with no change and possibly an increase of $\sim 30\%$ if the third epoch scaling is correct. This increase is also seen for [OII], though a larger slit width was used at the third epoch. At this epoch, the MMT spectrum did not have sufficient wavelength coverage to catch $H\beta$ /[OIII] so it is harder to draw firm conclusions on any trends here. The $H\beta$ broad component is redshifted by

~ 1300 km/s and MgII shows a smaller ~ 500 km/s redshift. CIII] shows a modest blueshift of ~ 250 km/s. There is no sign of an evolution in velocity offsets as seen for J084305. The CIII] and MgII line widths show the same trend as their amplitudes, as do the narrow lines, though $H\beta$ only shows an increase in width. Looking at the line profiles, CIII] shows a significant blue wing change whereas MgII sees a change on the red wing. It is perhaps interesting that [OII] sees an enhancement primarily on the blue wing. No clear spectral signature of a possible intervening galaxy has been detected.

3.3 J142232

The lightcurve for this target shows there has been a rise of approximately three magnitudes since the SDSS epoch and $|\Delta g| \simeq 1.22$ mag over the 6 spectral epochs as estimated from interpolation of the LT lightcurve. The SDSS epoch is faint and should therefore be treated with caution. The photometry shows this target to be evolving smoothly but there is a notable dip around 55500 MJD, this is after the assumed ‘peak’ around 55000 MJD. An earlier dip around 54200 MJD is also visible though the CRTS data show considerable scatter here. After the 56500 mark there is a rapid drop of ~ 1.1 mag/yr, the time of the spectral observations, but the most recent photometry shows this levelling off. The cadence of the LT observations is not always ideal which may affect the spectral scaling corrections (Sec. 2.3.3).

For this target, outside of the rest-frame UV ($\lambda_{\text{obs}} > 6400 \text{ \AA}$) no other spectral features or narrow emission lines were detected. Given a lack of detected narrow lines, the systemic velocity/redshift has been determined from the median MgII line centre. For clarity, the corresponding increase in uncertainty has been omitted from the plot in Fig. 3. Also, at this redshift the CIV line is seen, albeit very near the blue cutoff. Shortward of $\sim 3200 \text{ \AA}$ the flux calibration is less reliable due to the lack of calibration points for the chosen standard stars.¹

The spectroscopic results for J142232 are broadly similar to that seen in J084305/J094511. There is a factor ~ 4 drop in the continuum and the CIII]/CIV fluxes appear to track this change quite closely, dropping by a factor ~ 3 . The MgII flux also tracks the continuum to a lesser extent, dropping by a factor ~ 2 . The Fe component behaves similarly though there is a higher degree of scatter. The CIII] centre shows a blueshift of ~ 1000 km/s, which does not evolve, and the line gets narrower in decline. In contrast, MgII shows a higher degree of scatter in the velocity offset and an increase in line width of ~ 1000 km/s over this period. There is evidence for evolution of the line profiles, most notably on the CIII] blue wing MgII/CIV red wing.

In addition, there is also a set of strong narrow absorption features present, possibly evidence for an intervening galaxy. These features are consistent with MgII/Fe absorption at $z = 0.855$ and are highlighted in Fig. 5. The AGN is at $z = 1.076$. Alternatively, this feature may be the result of an outflow intrinsic to the AGN. If in outflow, this Δv is

¹ The fitting pipeline would occasionally fail to fit CIV and instead add an additional continuum component. To prevent this, the width of CIV was constrained to be the same as CIII] so the CIV results should be treated with caution.

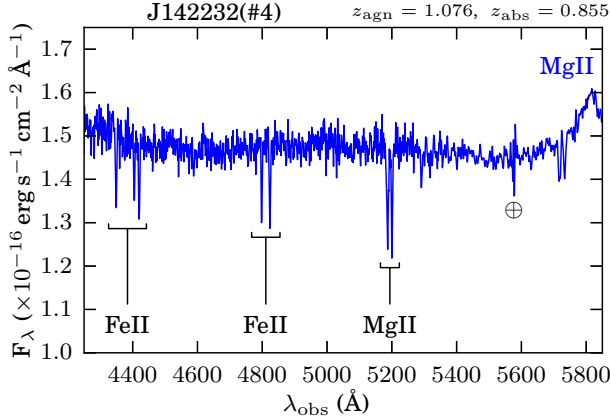


Figure 5. Fourth spectral epoch for J142232 highlighting the narrow absorption features seen. These are consistent with MgII/FeII absorption at a lower redshift or possibly an outflow intrinsic to the AGN. A similar MgII/FeII feature is seen nearer the blue wing of the MgII broad line though in this case only the MgII doublet is readily visible.

close to $0.1c$ which is much greater than the value of $0.01c$ typically used to distinguish between associated and intervening systems (York et al. 2006). There is also a second similar but fainter feature, seen nearer the blue wing of the MgII broad line. In addition, the SDSS epoch for this target is flagged as a possible blend, i.e. more than one peak was detected in a given filter. Given that the target was faint at this epoch this may not be reliable but lends further weight to the possible presence of an intervening galaxy.

3.4 J103837

This object exhibits the most complex lightcurve and the spectra have been scaled relative to the $[\text{OIII}]_{5007}$ flux (Sec. 2.3.3). There is evidence of at least three peaks with occasional rapid changes in brightness, particularly around 56300 MJD which shows a drop of ~ 0.4 mag over 2.5 months. Here the cadence of the LT photometry is less than ideal. It is possible the drop was larger than observed. After the drop it appears to rise more gradually at ~ 0.2 mag/yr though there is a spike in the data ($g = 19.79$ mag) at the third spectral epoch at 57137 MJD. There is a peak-to-peak change from the Sloan era of at least two magnitudes. The increase in complexity, coupled with the lack of LT data at the second spectral epoch causes a problem when attempting to correct the spectral data for transparency effects (Sec. 2.3.3). For this object, the $[\text{OIII}]$ flux was used to rescale the data as the interpolation using the LT data was poor. This may introduce additional errors if the line flux varies either intrinsically over this timescale or due to aperture/seeing effects.

Given that in this case the second spectral epoch represents the minimum, it is harder to draw conclusions regarding any spectroscopic trends. The SNR of the third epoch was sufficient to allow a more complex fit for the $\text{H}\beta/\text{MgII}$ lines. In this case two Gaussian profiles were used simultaneously. The CIII] results should be treated with caution as the bulk of the line was beyond the blue cutoff requiring that the line center and width be fixed relative to that of MgII. It was not reliably detected at the second epoch. Both

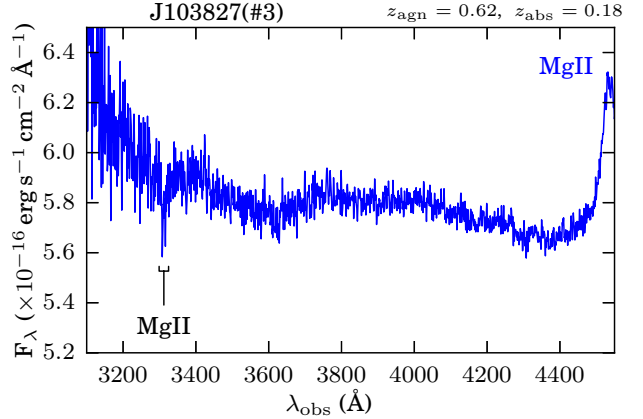


Figure 6. Third spectral epoch for J103837 highlighting the narrow absorption feature. It is consistent with an MgII doublet at a lower redshift than the AGN.

of the wider Gaussian components for $\text{H}\beta/\text{MgII}$ appear to undergo a blueshift over the period of observations and $\text{H}\beta$ shows evidence of an increase in FWHM also.

For this target, an absorption doublet was seen which may indicate the presence of an intervening galaxy. It is consistent with MgII at a low redshift and is highlighted in Fig. 6. This feature has only been reliably detected in the third epoch, likely due to the higher SNR achieved in the blue. Here the suspected absorber lies at $z = 0.18$ and is far less likely to be an outflow intrinsic to the AGN ($z = 0.62$) as might be the case for the absorption seen in J142232. If in outflow, the velocity would be in excess of $0.25c$ (i.e. $\gg 0.01c$). This is seen in some high-ionisation species but is perhaps implausibly high for these low-ionisation lines.

4 MICROLENSING MODELS: TECHNIQUES

This section will summarise the methods used for exploring the suggestion that these AGN transients are microlensing events. The results will be detailed in Section 5.

4.1 Point-source point-lens model

It is useful to first start with the simplest of cases, that of a point-mass lens and point-source with no external shear. This is likely an oversimplification but will nevertheless prove useful, particularly with regard to J084305 and J094511, both of which have lightcurves which are single-peaked and smoothly evolving (Fig. 2). In this model the magnification is given by:

$$\mu = \frac{y^2 + 2}{y\sqrt{y^2 + 4}}, \quad y := \beta/\theta_E \quad (2)$$

Here, y is the normalised source position in units of the Einstein radius of the lens which is given by:

$$\theta_E = \left(\frac{4GM}{c^2} \frac{D_{ds}}{D_d D_s} \right)^{1/2} \quad (3)$$

D_d , D_s and D_{ds} are the angular diameter distances

Table 4. Free parameters in the simple microlensing model.

parameter	description
M_l	lens mass
v_\perp	transverse velocity
t_0	midpoint epoch
z_d	lens redshift
y_0	impact parameter
F_s	source flux (pre-lensing)
F_b	background flux (unlensed)

for the lens, source and between the lens and source respectively. To compute the lightcurve $F(t) = \mu(t)F_s$ requires the formula for the trajectory of the source, as in [Wambsganss \(2006\)](#):

$$y(t) = \sqrt{y_0^2 + \left(\frac{t - t_0}{t_E}\right)^2}, \quad t_E := \frac{D_d \theta_E}{v_\perp} \quad (4)$$

where y_0 is the impact parameter at t_0 and v_\perp is the transverse velocity of the lens relative to the observer/source line of sight. The Einstein timescale, t_E defines a characteristic timescale for the lensing event. If one includes an additional background flux contribution from the host/lens galaxy, this model has seven free parameters. These are listed in Table 4.

In order to explore this model in more detail, **emcee**, a Bayesian model fitting package that uses a Markov chain Monte Carlo (MCMC) to explore parameter space was used ([Foreman-Mackey et al. 2013](#)). Gaussian errors are assumed and the parameters constrained to remain physical. In order to deal with the mass/velocity degeneracy in the model, a log-normal prior on the expected lens mass was used. This takes the form of a Chabrier IMF ([Chabrier 2003](#)) with an additional weighting factor M to account for the increase in lensing cross-section with mass. The lower limit for the lens mass was set at $10^{-3}M_\odot$ and the transverse velocity of the lens was left free. Over the course of a lensing event an AGN will also have some level of, as yet unknown, intrinsic variability. A simple approach that attempts to allow for this was to increase the errors on the photometry by an additional 10% of the flux level at each epoch, a fairly conservative estimate for typical AGN variability. The CRTS data were not used in this analysis due to concerns over colour effects resulting from the clear filter used.

Parameter constraints were obtained using the marginalised posterior probability distributions. For each, the peak value was determined by fitting a polynomial through the maximum of the distribution using a coarse sampling (logarithmic bins for M_l and v_\perp). A finer sampling of the distribution was used to determine the narrowest allowable range which encompassed $>68\%$ of the data about this peak. In addition, values for r_E , the Einstein radius in the source plane, were calculated from the MCMC trace output. This distribution (logarithmic bins) was then used to produce constraints in the same manner as for the other parameters. The results from our MCMC analysis will be displayed in 5.1.

4.2 Extended sources

The assumption of the AGN as a point source will not always be valid so it is necessary to consider extended source models. Indeed, this fact can potentially be exploited to yield additional information regarding the accretion disc (AD) and BLR structure. In order to explore extended source models in more detail an inverse-ray-shooting code technique ([Jiménez-Vicente 2016](#)) was used to construct magnification maps, initially for a point-lens model. The maps that have been constructed are normalised in units of the Einstein radius and have a pixel scale of $1/800 \theta_E$. A simplifying assumption is that the accretion disc and BLR sources are gaussian. This should be reasonable for low inclinations ($\phi < 45^\circ$) and disc-like morphologies when projected along the line of sight ([Mortonson et al. 2005](#); [Sluse et al. 2011](#)). For a given set of lens/source parameters, the lightcurve for the event is obtained by varying the source position under the magnification map as a function of time and integrating to find the total amplification at each epoch.

Our starting point for the testing of extended sources is to make use of the simplified thin-disc model from [Morgan et al. \(2010\)](#). This provides a simple formula for the effective disc size:

$$\log_{10} \left(\frac{R_{2500}}{\text{cm}} \right) = 15.184 + \frac{2}{3} \log_{10} \left(\frac{M_{\text{BH}}}{10^9 M_\odot} \right) + \frac{1}{3} \log_{10} \left(\frac{L_{\text{bol}}}{\eta L_E} \right) \quad (5)$$

where L_{bol} is the bolometric luminosity, η the accretion efficiency and L_E the Eddington luminosity. However, from the study of differential microlensing of components of strongly lensed quasars, [Morgan et al. \(2010\)](#) also found evidence that the AD is larger than this relationship implies, typically by a factor of a few. They derive the following empirical relationship:

$$\log_{10} \left(\frac{R_{2500}}{\text{cm}} \right) = 15.78 + 0.8 \log_{10} \left(\frac{M_{\text{BH}}}{10^9 M_\odot} \right) \quad (6)$$

Both of these relationships require an estimate for the mass of the black hole. For this, we make use of the [McLure & Dunlop \(2004\)](#) single epoch relation:

$$\frac{M_{\text{BH}}}{M_\odot} = 3.2 \left(\frac{\lambda L_{3000}}{10^{37} \text{W}} \right)^{0.62} \left[\frac{\text{FWHM}_{\text{MgII}}}{\text{km s}^{-1}} \right]^2 \quad (7)$$

This gives the black hole mass as a function of MgII line width and luminosity at 3000Å. This relationship depends on accurate estimates of the monochromatic continuum luminosity and MgII width. Both may be overestimated if there is an ongoing microlensing event. The black hole mass estimates for each epoch are listed in Table A1. For Equation 5, the bolometric luminosity was calculated using the monochromatic luminosity (λL_{2500}), from the same epoch as the black hole mass estimate, along with a bolometric correction factor of 5.6 ([Elvis et al. 1994](#)). The accretion efficiency was assumed to be 0.1. Finally, the gaussian sources for testing with the magnification maps are generated with a 2σ radius equivalent to the accretion disc size estimates obtained above.

An important test of our extended source model is to see if it can reproduce the analytic lightcurve from the point source model in the limit when the source size is very small.

This is achieved by setting the size of the source to a single pixel and testing a wide range of impact parameters. The results are in excellent agreement, even for very small impact parameters, and implies that pixel/resolution effects should be minimal as long as source sizes larger than the pixel scale are used.

Sources larger than the accretion disc estimates, which are more appropriate when considering BLR emission, are also considered. The results of the extended source analysis are displayed in Section 5.2.

4.3 External shear due to lens host galaxy

For the models we have discussed so far, the assumption of a point-mass lens is reasonable as it is assumed the lensing is caused by a single star. However, this neglects the presence of an external shear due to the lens host galaxy which can have significant consequences. This background perturbation breaks the circular symmetry of the point-mass lens and results in the degenerate point in the source plane unfolding into a caustic pattern of varying complexity. The corresponding lightcurve may exhibit double peaks and more complex structure as a result. It should be noted that some microlensing events will also involve additional stars along the line of sight which can have a similar effect. If the lensing galaxy is small, this becomes less likely, though some events may also involve binary systems (L16).

One model for describing the effect of microlensing plus an external shear is that of the Chang-Refsdal (CR) lens (Chang & Refsdal 1984). This is a useful starting point as it treats the lens-host galaxy as an additional point mass nearby. The shear parameter is defined as the ratio of the Einstein radius of the galaxy to the distance of the stellar lens from the galaxy center, all squared. If this ratio is greater than unity, there can be strongly de-magnified regions in the source plane. This adds a further layer of complexity when considering the lightcurves. For very small shear values, the magnification map is essentially the same as for an isolated point lens. For shear values > 2 , the two caustic regions continue to grow further apart whilst decreasing in extent.

Figure 7 shows how the shear varies in relation to the lens galaxy mass for selected star-galaxy separations. This assumes a lens redshift of 0.2 and source redshift of 1.0. L16 estimates that an AGN will have a foreground galaxy present in perhaps 0.2% of cases but only a small fraction of these will have an ongoing high-amplitude microlensing event at any one time. We appear to be in a regime where some events will be well approximated by a point lens and others will require a more detailed treatment of the perturbing lens galaxy.

The use of a CR magnification map (Fig. 11) allows a qualitative explanation for the double-peaked lightcurve seen for J142232 and the result is displayed in Section 5.3.1. Given that this model is perhaps an oversimplification, a thorough treatment of the CR lens, and other more complex lensing models is deferred to a later paper.

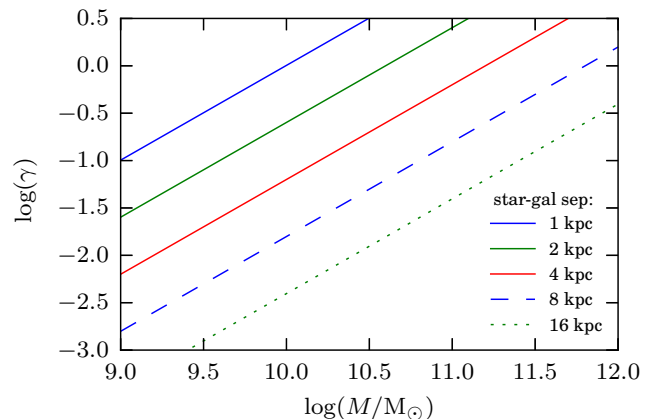


Figure 7. Plot of the Chang-Refsdal shear parameter, γ , against galaxy mass for selected star-galaxy distances. Here, the lens redshift is assumed to be 0.2 and the source redshift 1.

5 MICROLENSING MODELS: RESULTS

In this section, the results from the analysis of the various microlensing models are presented. First is the point-source point-lens model MCMC analysis. This performs well for the two single-peaked targets, J084305 and J094511. Secondly, the extended source model is applied to the same targets. While not a full exploration of parameter space, this allows us to place some constraints on the size of the emitting region for CIII], particularly for J084305. Finally, an initial exploration into the more complex case of microlensing with an external shear is made for J142232 and J103837.

5.1 Point-source point-lens model

5.1.1 J084305

The microlensing parameter estimates for J084305 are shown in Table 5 and the marginalised parameter model fit to the data is shown in Fig. 2. The full MCMC results are displayed in Figure A5. Here, one can see there is a strong correlation of lens mass with transverse velocity, as expected, and also with impact parameter vs the pre-lensed AGN (or ‘source’) flux. An anti-correlation is seen for the background flux with respect to both impact parameter and source flux. The model lightcurve produces a fit to the data with a reduced chi-squared value of 0.69. This assumes a negligible background component and has been calculated using the same photometric errors as that for the MCMC analysis. Given the good fit to the data, this model was used to scale the spectra. This specific model has an Einstein radius of 12.1 light-days, Einstein timescale of 7.5 years and a peak amplification of 10.3.

Though poorly constrained, the values obtained for the lens mass ($0.37 M_{\odot}$), transverse velocity (830 km/s) and redshift (0.34 as compared to 0.895 for the AGN) are all physically reasonable. The estimate for the background flux from the host/lens galaxies is consistent with an upper limit ($g \leq 23.6$ mag) and the AGN would have an unlensed magnitude of $g \approx 22.3$ mag.

Table 5. Parameter estimates obtained from the MCMC analysis, including the Einstein radius in the source plane, for J084305. The model using these marginalised parameters, assuming a negligible background flux, produces a fit to the data with a reduced chi-squared value of 0.69 and has an Einstein radius of 12.1 light-days. Parameter definitions as per Table 4.

J084305		$z_{\text{agn}} = 0.8955$
parameter	value	unit
z_d	$0.34^{+0.27}_{-0.21}$	
M_l	$0.37^{+1.19}_{-0.29}$	M_\odot
v_\perp	830^{+1080}_{-510}	km s^{-1}
y_0	$0.097^{+0.026}_{-0.031}$	θ_E
t_0	56137^{+23}_{-23}	MJD
F_s	$5.5^{+1.5}_{-1.6}$	$\times 10^{-18} \text{erg s}^{-1} \text{cm}^{-2} \text{\AA}^{-1}$
F_b	< 1.8	$\times 10^{-18} \text{erg s}^{-1} \text{cm}^{-2} \text{\AA}^{-1}$
r_E	$10.5^{+17.0}_{-6.3}$	light-days
$r_{E,\text{mp}} = 12.1 \text{ l.d.}$		$\chi^2_\nu = 0.69$

Table 6. Parameter estimates obtained from the MCMC analysis, including the Einstein radius in the source plane, for J094511. The model using these marginalised parameters, assuming a negligible background flux, produces a fit to the data with a reduced chi-squared value of 1.14 and has an Einstein radius of 12.8 light-days. Parameter definitions as per Table 4.

J094511		$z_{\text{agn}} = 0.758$
parameter	value	unit
z_d	$0.29^{+0.24}_{-0.18}$	
M_l	$0.40^{+1.47}_{-0.32}$	M_\odot
v_\perp	580^{+950}_{-360}	km s^{-1}
y_0	$0.074^{+0.033}_{-0.029}$	θ_E
t_0	55816^{+26}_{-26}	MJD
F_s	$4.3^{+1.8}_{-1.8}$	$\times 10^{-18} \text{erg s}^{-1} \text{cm}^{-2} \text{\AA}^{-1}$
F_b	< 1.8	$\times 10^{-18} \text{erg s}^{-1} \text{cm}^{-2} \text{\AA}^{-1}$
r_E	$11.9^{+18.9}_{-7.2}$	light-days
$r_{E,\text{mp}} = 12.8 \text{ l.d.}$		$\chi^2_\nu = 1.14$

5.1.2 J094511

The microlensing parameter estimates for J094511 are shown in Table 6 and the marginalised parameter model fit to the data is shown in Fig. 2. The model lightcurve produces a fit to the data with a reduced chi-squared value of 1.14. This specific model has an Einstein radius of 12.8 light-days, Einstein timescale of 10.8 years and a peak amplification of 13.5. The CRTS data was not used in the analysis but is in broad agreement with the model. The accuracy of the model may be adversely affected due to the extra structure seen in the lightcurve at later epochs (MJD > 57000).

Similarly to J084305, the same correlations are seen and the parameter estimates are physically reasonable. In this case, the transverse velocity and impact parameter are lower. Using these parameter estimates, the Einstein timescale is 10.8 years, Einstein radius 12.8 light-days and the peak amplification factor is 13.5. The estimate for the unlensed flux level from the host/lens galaxies is consistent with an upper limit ($g \leq 23.6 \text{ mag}$) and the AGN would have an unlensed magnitude of $g \approx 22.6 \text{ mag}$.

Table 7. Extended source sizes and Einstein radii for J084305 using the lensing model parameters in Table 5. The sources are gaussian and the numbers shown here reflect the 2σ radius. The accretion disc sizes have been calculated as per Section 4.2. The CIII] and MgII sizes have been determined from the spectroscopic data as per Section 5.2.1. The errors here reflect the fitting process only.

source	size (light-days)	(θ_E)
thin disc	0.19	0.016
morgan disc	0.91	0.075
CIII]	4.8 ± 0.2	0.40 ± 0.02
MgII	> 15	> 1.24

5.2 Extended source models

The preceding section provides good evidence that the point-source, point-lens microlensing model is a reasonable approximation for the continuum changes seen in J084305 and J094511. We now explore these lensing models in the regime where the point-source approximation no longer applies. This is particularly important with regards to the size of the BLR. The spectroscopic analysis shows there is evidence for the differential evolution of the BLR fluxes, namely MgII and CIII], with respect to the continuum. If these lines are partially resolved by the lens then it allows constraints to be placed on the size of the emitting region. Indeed, in the case of J084305 in particular, there is evidence to suggest that the CIII] region is compact enough to undergo significant changes in amplification as the lensing event unfolds.

5.2.1 J084305

As a starting point for testing, the lens model parameters listed in Table 5 have been used. The results of the extended accretion disc testing are shown in Fig. 8. Here the gaussian sources representing the thin disc and Morgan disc sizes, calculated as per Section 4.2, are shown in comparison with the point-source model. The sizes used are listed in Table 7. It is clear from the figure that there is little separation between the two models except during the midpoint of the event. Here, the increased amplification seen at the peak for the Morgan disc is likely a result of the source being of a suitable size to have significant flux overlapping the regions of highest magnification for the given the impact parameter. The fit for the thin disc model has $\chi^2_\nu = 0.70$ and for the Morgan disc $\chi^2_\nu = 0.88$. For lensing models with a smaller projected Einstein radius (varying z_d , M_l , v_\perp appropriately), the distinction between the two models becomes more apparent, favouring the thin disc model. Conversely, for larger Einstein radii, both models converge to the point-source solution. Given that the point-source model performs well for this target, it is not particularly surprising that smaller sources provide a better fit to the data i.e. the accretion disc is largely unresolved. Due to computational limitations and the uncertainty in the Einstein radius, a full exploration of the available parameter space has not yet been performed.

Conversely, there are indications that the BLR is being resolved by the lens. Figure 9 shows the flux evolution for selected source models, relative to the first spectroscopic epoch, against the observed data for CIII] and MgII. Again,

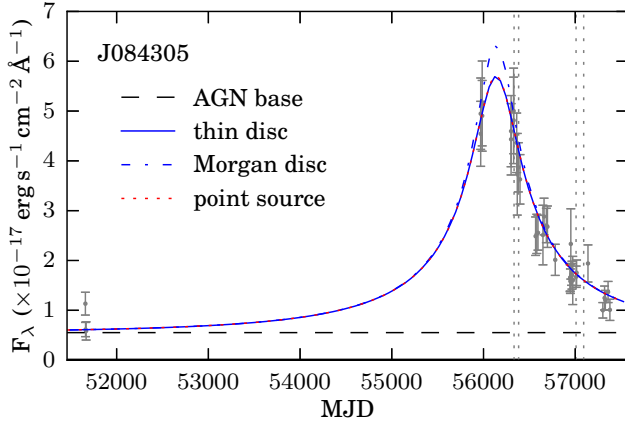


Figure 8. Extended source model lightcurves for J084305. The grey data are the original photometry points and the vertical lines are the spectral epochs. The source sizes are listed in Table 7. The dashed line represents the AGN base flux.

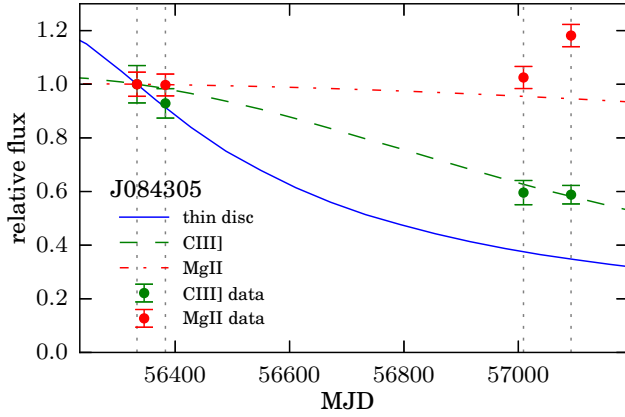


Figure 9. Evolution of extended model fluxes relative to the first spectral epoch. Overplotted are the spectroscopic measurements of CIII] and MgII. The source sizes are listed in Table 7.

note the differential evolution of the lines with respect to the continuum. If one assumes this is a lensing effect, the data for CIII] is sufficient to allow a determination of the size of the emitting region using a χ^2 distribution, assuming gaussian errors. The values are noted in Table 7. Given the uncertainty in the Einstein radius of the lens, the relative size of $0.4 \theta_E$ should prove more robust than the absolute size. For this particular lens model the absolute size of the CIII] emitting region is 4.8 ± 0.2 light-days. The true value is likely to be in the range ~ 2 –11 light-days when the increased uncertainty due to the lens model is taken into account. In the case of MgII, the data is consistent with no change or perhaps a late increase in flux. A source size greater than approximately 15 light-days (or $> 1.2 \theta_E$) would see little evolution in flux over this period. This provides a lower limit to the size of the MgII emitting region. It does not explain the jump in flux seen for the fourth epoch. However, this could be due to a scaling problem. As will be discussed below, the estimate for the size of the CIII] emitting region is relatively compact when compared with size predictions for the CIV and H β regions.

Table 8. Extended source sizes and Einstein radii for J094511 using the lensing model parameters in Table 6. The sources are gaussian and the numbers shown here reflect the 2σ radius. The accretion disc sizes have been calculated as per Section 4.2.

source	size (light-days)	(θ_E)
thin disc	0.097	0.0076
morgan disc	0.31	0.024

Table 9. Extended source sizes and Einstein radii for J142232 using the lensing model parameters in Section 5.3.1. The sources are gaussian and the numbers shown here reflect the 2σ radius. The accretion disc sizes have been calculated as per Section 4.2.

source	size (light-days)	(θ_E)
thin disc	0.23	0.036
morgan disc	0.83	0.13

5.2.2 J094511

J094511 shows similarities to that of J084305. The accretion disc estimates, using the lensing model parameters in Table 6, provide lightcurves which are nearly indistinguishable from the point-source case. The sizes obtained are listed in Table 8. For this target, the uncertainty on the scaling of the third epoch means that it is not yet possible to place reasonable constraints on BLR sizes. What can be said for this object is that if the observed changes are due to microlensing, then the size of the CIII] region again has to be small, perhaps on the order of ~ 1 light-day as this line appears to track the continuum closely.

5.3 Lensing plus external shear

5.3.1 J142232

A detailed analysis of more complex lensing morphologies is beyond the scope of this paper, but an exploratory analysis is presented here in order to address the question of whether or not the double- or indeed multiply-peaked lightcurves seen in this sample can also be due to microlensing.

J142232 exhibits a clear double-peak in the lightcurve which requires the use of a more complicated magnification map in order to try and reproduce this. For this test, a CR lens (Sec. 4.3) with the external shear parameter set to 0.05 was used. With reference to Fig. 7, this value is reasonable for smaller galaxies with a star-galaxy separation ~ 4 kpc. It is enough to unfold the central degenerate point into a diamond-like caustic region. For this target, there is also a possible lens redshift due to the presence of absorption features in the spectrum. Using this and an assumed lens mass of $0.5 M_\odot$ gives this particular lens model an Einstein radius at source of ~ 6.24 light-days. As for J084305, two accretion disc size estimates were used and these sizes noted in Table 9. Next, the source track and intrinsic flux were varied to provide the qualitative lightcurves seen in Fig. 10. The magnification map and source/track used in this model are shown in Fig. 11.

It is worth noting that the larger Morgan disc does not resolve the double-peak structure that is seen for the thin disc. The thin disc model fit to the data is poor around 54000

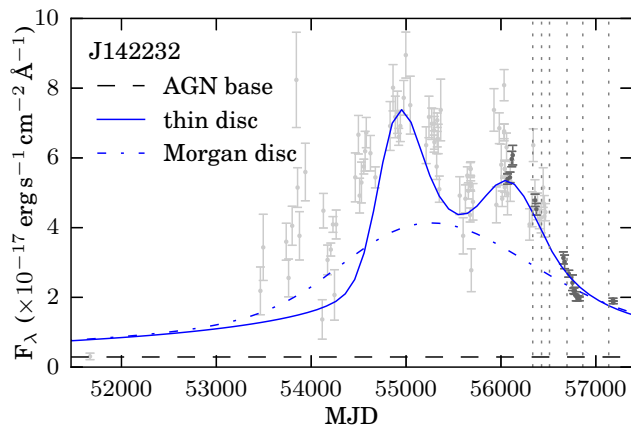


Figure 10. Chang-Refsdal lens model lightcurves for J142232. The grey data are the original photometry points, the darker points are the LT epochs. The source sizes are listed in Table 9. The dashed line represents the AGN base flux.

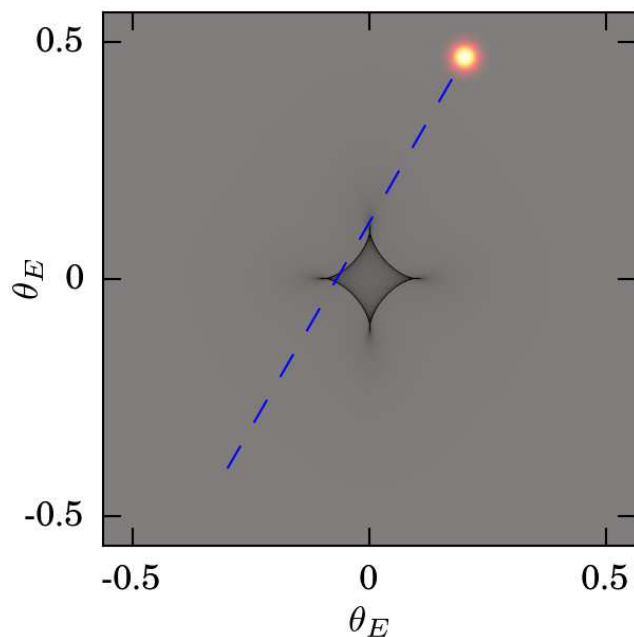


Figure 11. Magnification map and source/tracks to produce the thin disc lightcurve shown in Fig. 10.

MJD but the CRTS data (points prior to ~ 56000 MJD) are less reliable at these fainter magnitudes. It is also possible that the single Sloan epoch of $g = 23$ mag is not reliable and that the clear CRTS filter will introduce colour effects. These caveats aside, this lens model does provide a plausible explanation for the double-peaked structure seen in J142232 but requires refinement before any further conclusions can be drawn. As with J084305 and J094511, there is evidence to suggest that the BLR emission regions, particularly CIII] but also MgII in this case, are compact enough to show significant amplification changes on these timescales.

5.3.2 J103837

In the case of J103837 there is even more complexity in the lightcurve. The example used for J142232 allows a fit to double-peaked lightcurves, but to explain the three peaks seen for this object likely requires a more complex scenario. A binary lens, or one involving multiple point-masses, could generate the required caustic pattern to reproduce the peaks seen. There is spectroscopic evidence for an intervening system at $z = 0.18$. Assuming a single lens mass of $0.1M_{\odot}$, this projects to an Einstein radius of ~ 8 light-days. The thin disc size estimate, based on the faintest of the three observed epochs is ~ 0.1 light-days. This suggests that the accretion disc is likely to be unresolved but requires a more realistic lensing model. This will be the focus of future work.

6 DISCUSSION

The AGN transients in this paper have been selected because they are candidates for microlensing events. The photometry shows a minimum of a factor five increase in luminosity and a smooth evolution on year-long timescales. For three of the objects, the spectroscopy reveals differential evolution in the broad line fluxes with respect to the continuum. In particular, CIII] is seen to track the changes in the continuum more closely than that of MgII. Two objects also show spectroscopic signatures indicating the possible presence of an intervening galaxy. A simple point-source/point-lens model produces a reasonable fit to the bulk continuum changes seen for the single-peaked events. When extended source models are included for the BLR, the differential changes seen in the broad lines can be interpreted as the BLR being partially resolved by the lens. This implies that the CIII] emitting region is smaller than that for MgII and the data for J084305 allows size constraints for these regions on the order ~ 2 – 11 light-days. More complex lensing models are required to produce lightcurves displaying multiple peaks.

Having summarised our results so far, we now put them into context of what we know about AGN, discuss whether they make sense and what we might learn from them. The focus for this discussion will be on the microlensing hypothesis. Other plausible scenarios include: tidal disruption events; accretion disc instabilities; and extinction events. These are considered in more detail in L16. Target J142232 also has X-ray data available. Collinson (2016)[submitted] shows that, based on the broadband SED, a lensing scenario is consistent with the data.

6.1 Continuum variability

Can the variability of the AGN in this paper be described as typical? In the context of the wider AGN population, long-term optical variability is commonly described in terms of a damped-random-walk (DRW) model (Kelly et al. 2009; MacLeod et al. 2010, 2012). It quantifies the variability using a structure function which gives the rms magnitude difference as a function of time lag between different epochs. This model performs well when applied to large quasar samples. The two key parameters are the damping or characteristic timescale, τ , and the asymptotic rms magnitude difference at the longest timescales, SF_{∞} . We obtain the

Table 10. Damped random walk parameters obtained for J084305 and J094511. The values have been computed for the observed data and the residuals after subtraction of the microlensing model.

	J084305		J094511	
	observed	residual	observed	residual
SF_{∞}	1.62	0.21	2.19	0.26
$\log(\tau)$	3.72	1.96	3.94	2.28

DRW parameters for J084305 and J094511 in two situations. First, for the original lightcurve and second, for the residual lightcurve after taking the microlensing model into account. The values obtained are displayed in Table 10.

With reference to MacLeod et al. (2010, Table 2), it is clear the DRW parameter values for the observed data are atypical for quasars and may even be biased due to a different underlying process describing the observed variability (Kozłowski 2016). However, after taking the microlensing models into account, the parameters ($\log(\tau) \sim 2$, $SF_{\infty} \sim 0.2$) are much more typical for quasars. A typical DRW origin for the bulk variability in these objects cannot be conclusively ruled out but this does lend further credence to the microlensing hypothesis. Regardless of the physical model it is notable that, after removing the trend, they look normal.

The underlying mechanism responsible for typical AGN variability is thought to be related to accretion disc thermal instabilities and/or reprocessing of X-ray/UV emission (Kelly et al. 2011; Shappee et al. 2014; Edelson et al. 2015). There may also be reprocessing of FUV emission due to optically thick clouds on the inner edge of the BLR. This can reproduce some of the observed UV/optical lags (Gardner & Done 2016) and can also address issues in relation to observations of the UV bump (Lawrence 2012). In effect these clouds would give rise to a ‘pseudo-continuum’ component which may prove important when testing various surface brightness profiles relating to the accretion disc and BLR. It has been suggested that the variability seen in luminous quasars on long timescales may be primarily due to ongoing microlensing (Hawkins 2002).

6.2 Accretion Disc: point-source or extended?

Is the point-source/point-lens model an oversimplification? It works well for J084305/J094511, indicating that in these cases the accretion disc is sufficiently small with respect to the lens footprint that it goes unresolved. A drawback of the model is that it potentially biases the results towards lensing systems which favour smaller accretion disc sizes and thus limits the amount of useful information which can be extracted regarding the disc. For example, when extended AD models are considered, we are unable to differentiate between a standard thin-disc and the Morgan et al. (2010) prediction. Nonetheless, it is likely that there will be cases where the accretion disc is resolved to a certain extent. Here the point-source model will fail and the ability to differentiate between accretion disc models of varying size will become easier. In this work we have also made the simplifying assumption that the accretion disc surface brightness profile can be treated as a gaussian, with a 2σ radius equivalent to the radii calculated in Equations 5 & 6. This should prove reasonable as Mortonson et al. (2005) state that microlens-

ing fluctuations are relatively insensitive to all circular disc model properties with the exception of the half-light radii.

The microlensing of a point-source is expected to be achromatic but there is evidence of a colour change, as seen in the UV power-law slopes, for these objects at later epochs (Table A1). If this is to be explained in the context of microlensing then it may indicate that the accretion disc is at least partially resolved by the lens and the point-source approximation is invalid. The observed colour changes would be sensitive to the temperature profile of the disc and also any caustic structure in the lens configuration. Alternatively, changes in amplification between the disc and a more extended ‘pseudo-continuum’ cloud component could also produce a colour change though this possibility has not yet been fully explored (Lawrence 2012). At later epochs host/lens galaxy contamination may also need to be accounted for. For J084305/J094511, the estimate for the expected host/lens galaxy contribution is at least a factor of 2-3 below the AGN base level in the g-band. This goes some way to explaining why the detection of lens galaxy signatures in the spectra for these objects has proven difficult. A further consideration is the effect of any broad line flux intruding into the filters used in the observations, particularly with respect to MgII in the g-band, perhaps more an issue for J094511.

6.3 BLR

With the simplifying assumption that the variability in the broad lines is entirely due to lensing, the differential changes between the continuum, CIII] and MgII fluxes seen in three of the targets suggest that the BLR is at least partially resolved. Indeed, for J084305 the data is sufficient to allow constraints on the size of the CIII] emitting region. The size estimate from our model is ~ 5 light-days with an expected range of $\sim 1.7 - 11$ light-days when taking account of the uncertainty in the Einstein radius of the lens. These sizes reflect the 2σ radii used in our extended source modelling. Converting to half-light radii yields $\sim 1.0 - 6.5$ light-days which is surprisingly small when compared with BLR radius estimators. One example is from Bentz et al. (2009) for H β and another from Kaspi et al. (2007) for CIV. Using these, after obtaining a continuum luminosity for J084305 from the 4th epoch UV power-law and correcting for the lensing amplification, we obtain a radius of 34 and 31 light-days for H β and CIV respectively. Given these values, one would expect CIII] to perhaps be at least comparable in size, if not a factor of up to two larger than that seen for CIV. Thus our size estimates appear surprisingly small.

For comparison with other observations, there are a handful of published lags for CIII] which have been determined from reverberation mapping. These serve as a proxy for BLR radius and some notable results include Peterson & Wandel (1999); Onken & Peterson (2002); Metzroth et al. (2006); Trevese et al. (2014). Most are for low redshift/luminosity targets and show CIII] to be on the order of 3.5-30 light-days for these objects, with a considerable degree of uncertainty. The high luminosity quasar in Trevese et al. (2014) has a much larger radius on the order of 270 light-days. For J084305 we estimate, after correcting for the lensing amplification, a bolometric luminosity for the AGN of $\log(L_{\text{bol}}) \sim 44.7$. This is at the lower-luminosity end of published lags but again suggests that our estimate is

intriguingly small. Of particular interest is the result from [Sluse et al. \(2011\)](#), where a radius for CIII] has been estimated based on the microlensing of a multiply-imaged quasar. Here, a multi-component fit to the CIII] profile provided evidence that the broadest components lie closer to the accretion disc and are therefore more affected by microlensing. In relative terms, their broadest component (for CIII] and CIV) is around 4 times larger than the continuum emitting region. The narrowest component is around a factor of 25 larger. Thus, our estimates for the CIII] region in J084305, though small, may in fact be dominated by the changes in the inner component. Thus far we have only used a single component for the CIII] region, partly due to SNR issues. It remains to be seen if a multi-component fit performs well. A further consideration is the morphology of the CIII] region. Reverberation mapping is sampling in the radial direction whereas microlensing provides a transverse sampling. Perhaps the CIII] region is more compact along certain lines of sight than reverberation mapping implies.

For J084305, in contrast to CIII], the MgII flux is consistent with no change. This implies that this region is more extended and therefore will not exhibit significant changes over the timescale of our observations. The lower size limit obtained is based on a single component to the line. As with CIII], it is possible that there is a broad component which is changing but this will require a more detailed treatment. [Sluse et al. \(2012\)](#) show that both CIII] and MgII exhibit changes due to microlensing in a sample of multiply-imaged quasars. They see evidence that the BLR is in general not spherically symmetric and that a bi-conical outflow model may not be appropriate in these cases. These systems benefit from the additional information supplied by the resolvable quasar images.

Thus far it has been assumed that the variability seen in the broad lines is entirely due to lensing but a more realistic scenario must include some intrinsic variability over the period of our observations. It may also be possible that, rather than being resolved by the lens, the observed broad line changes are entirely intrinsic to the AGN. Taking the MgII line as an example, [Sun et al. \(2015\)](#) see significant variability in this line ($\sim 10\%$) on ~ 100 day timescales. The amplitude of lightcurve variability seen in MgII also correlates with that seen in the continuum. Some reliable reverberation lags for MgII are reported in [Shen et al. \(2016\)](#) but a clear correlation with luminosity is not always apparent. In other cases MgII is unresponsive to continuum changes ([Cackett et al. 2015](#)) but on longer timescales MgII does appear to respond to large changes in continuum flux ([MacLeod et al. 2016](#)). In the case of J084305 and J094511 the MgII line does not seem to respond to the continuum drop even on these long timescales. Given that the MgII line should be at least partially dependent on the ionising continuum this is perhaps surprising. Lensing as an extrinsic cause for the continuum variability provides a natural solution however.

6.4 Lensing system

For the two objects where the simple lensing model performs well it is unfortunate that, as yet, there are no confirmed signatures of the presence of a lensing galaxy. One way of improving the constraints on the lens parameters would be

to include a prior on the transverse velocity of the lens in the MCMC analysis. For now, this parameter has been left free as a useful check on the validity of the results. The predicted values for the velocity are reasonable though perhaps a little high, particularly for J084305 with $v_{\perp} = 830^{+1080}_{-510}$ km s $^{-1}$. If the lens is at a low redshift then the transverse velocity for this target can be dominated by the peculiar velocity component of the lens galaxy and values this high are not completely unreasonable ([Mosquera & Kochanek 2011](#)).

Another consideration is the presence of strong lensing effects due to the suspected lens galaxy. Thus far this has been assumed to be negligible. An additional complexity is the possibility that there may be multiple AGN images, as yet unresolved, of which only one will be undergoing a high-amplitude microlensing event. This has the potential to affect our estimates for the AGN baseline luminosity. A more realistic microlensing scenario also requires a minimal external shear due to the lens galaxy and/or the possible influence of other lenses in the magnification map. That the simple model works well for two targets suggests that the suspected lensing galaxy may be of low mass or sufficiently distant so as not to affect the magnification map to any great extent.

6.5 Future work

One major drawback of this sample is that it is currently very difficult to remove any intrinsic AGN variability, preventing tighter constraints on the lensing parameters. This is possible for a number of multiply imaged quasars, where the time delays between images are short enough that intrinsic variations can be corrected for. For these there is also a known lens galaxy. In contrast, our objects are among the lowest luminosity and lowest redshift AGN lensing candidates known. The SDSS i-band magnitudes for J084305/J094511 are 20.98/21.11 mag (DR12 cModelMag) respectively, comparison with [Mosquera & Kochanek \(2011\)](#) shows there are only four targets at $z < 1$ and 10/87 with $i > 20$ mag. Whilst it may not be possible to disentangle the intrinsic AGN variability from the observations, these low luminosity targets do allow for a greater chance of observing larger amplitude changes in the BLR. In addition, the lensing models used for these objects may prove to be comparatively simple when compared to those involving massive elliptical lensing galaxies.

A priority for the future is to obtain high-resolution imaging of these targets in order to ascertain if there is evidence of any strong lensing or indeed the lens galaxy itself. There is also a good prospect of detecting many more lensed AGN candidates from long-baseline photometry. In addition, the slow evolution and high amplitude maximise the chances for obtaining follow-up observations of each event. For J084305/J094511, the models give an Einstein time of 7.5/10.8 yr and peak magnification factor for the continuum of 10.3/13.5 respectively. Long-term surveys should provide the opportunity to select targets on the slow rise to a high-amplitude microlensing event and allow ample time to plan follow-up observations accordingly. It would prove invaluable to monitor one of these microlensing events with a cadence that allows reverberation mapping to be performed simultaneously.

It is likely that more of the objects in our larger,

highly-variable AGN sample are also undergoing microlensing events. For some, the simple model again provides a good fit to the data though their slow evolution meant that they were not included in this paper. Other targets are excellent candidates for microlensing events in which the accretion disc may be well resolved by the lens. These, as with J142232/J103837, require a more thorough analysis in order to fully address these questions. More complex magnification maps, such as those available through the GERLUMPH database (Vernardos et al. 2015) should also be considered. In addition, incorporating all available photometry bands into the analysis is a high priority for future work.

If the microlensing interpretation is correct, this provides a valuable way of probing the inner regions of AGN. This technique is already being used for strong-lensed, multiply-imaged quasars (Sluse et al. 2012, 2015). If the lens-host galaxy is small and the event is due to a single stellar lens, these objects will be in a different regime to their multiply-imaged cousins. This, coupled with the fact that they are high-amplification events evolving over year-long timescales, also allows a coordinated observational strategy. As the microlensing event unfolds, it can provide a transverse sampling of the BLR, perhaps even the accretion disc. The shorter-timescale variability allows a probe of the radial structure via reverberation mapping. These high-amplitude microlensing events may be unique opportunities for mapping the inner structure of an AGN.

7 CONCLUSION

In summary, we have analyzed four extreme AGN transients, selected as candidates for rare, high-amplitude microlensing events. The lightcurve information, primarily from the LT and supplemented by data from Pan-STARRS and SDSS has allowed a detailed MCMC analysis of a simple point-lens point-source model. This model has proven to be an excellent fit to the data in the two single-peaked cases, J084305 and J094511. After removing the signal due to microlensing, the long-term variability in these objects appears much more typical of the wider AGN population.

The multi-epoch spectroscopy from the WHT has also provided valuable insight into these events. All four targets display differential variability of the broad line fluxes with respect to the continuum. In three objects the CIII] flux is seen to track the continuum closely whereas the MgII flux is less responsive to these changes or shows signs of no change at all. Using the working lensing models and the simplifying assumption of gaussian surface brightness profiles, the changes can be interpreted as being due to regions of differing size being affected by the lensing event to a different extent. The continuum emission can be treated as a point-source and the CIII] region is more compact than for MgII. In the case of J084305 the data also allowed size constraints to be placed on these regions.

The two objects not well described by the simple lensing models are J142232 and J103837. In both cases there is evidence for an intervening absorber, suggestive of the presence of a lensing galaxy. It is clear that the extra structure in the lightcurve for these double- or multiply-peaked events, requires a more complex lensing scenario to describe the event. This will likely involve the presence of additional

lens masses and/or external shear with the resulting caustic network giving rise to the features seen in the lightcurves. Any thorough analysis of these more complex models will also require consideration of extended sources, both for the accretion disc and BLR. Current limitations have meant that this will be left for future work but microlensing is still the favoured scenario for the long-term variability seen in these objects.

Future time-domain surveys will be an invaluable source of microlensing events of this type. A challenge to overcome will be in identifying the gradual trends over a year or more that might indicate a high-amplitude event is imminent. If possible, this will may allow sufficient time to coordinate an observing strategy, particularly with regard to reverberation mapping. The amplification, by an order of magnitude or more, of a higher-redshift, lower-luminosity AGN would be an ideal candidate for an RM study. This, combined with a detailed lensing analysis allows an unprecedented opportunity for probing the inner regions of these AGN. They are in a different regime, but wholly complimentary, to the microlensing studies in more luminous, multiply-imaged AGN. We must make the most of these opportunities whenever they arise.

ACKNOWLEDGEMENTS

AB acknowledges the support of the University of Edinburgh via the Principal’s Career Development Scholarship. Thanks also to Marianne Vestergaard for providing the FeUV template and to Jorge Jiménez-Vicente for supplying the base microlensing IRS code which we adapted for use in the extended model testing.

The Pan-STARRS1 Surveys (PS1) have been made possible through contributions of the Institute for Astronomy, the University of Hawaii, the Pan-STARRS Project Office, the Max-Planck Society and its participating institutes, the Max Planck Institute for Astronomy, Heidelberg and the Max Planck Institute for Extraterrestrial Physics, Garching, The Johns Hopkins University, Durham University, the University of Edinburgh, Queen’s University Belfast, the Harvard-Smithsonian Center for Astrophysics, the Las Cumbres Observatory Global Telescope Network Incorporated, the National Central University of Taiwan, the Space Telescope Science Institute, the National Aeronautics and Space Administration under Grant No. NNX08AR22G issued through the Planetary Science Division of the NASA Science Mission Directorate, the National Science Foundation under Grant No. AST-1238877, the University of Maryland, and Eotvos Lorand University (ELTE) and the Los Alamos National Laboratory.

The Liverpool Telescope is operated on the island of La Palma by Liverpool John Moores University in the Spanish Observatorio del Roque de los Muchachos of the Instituto de Astrofísica de Canarias with financial support from the UK Science and Technology Facilities Council.

The William Herschel Telescope is operated on the island of La Palma by the Isaac Newton Group in the Spanish Observatorio del Roque de los Muchachos of the Instituto de Astrofísica de Canarias.

REFERENCES

- Ahn C. P., et al., 2012, *ApJS*, **203**, 21
- Bentz M. C., et al., 2009, *ApJ*, **705**, 199
- Blackburne J. A., Pooley D., Rappaport S., Schechter P. L., 2011, *ApJ*, **729**, 34
- Cackett E. M., Gültekin K., Bentz M. C., Fausnaugh M. M., Peterson B. M., Troyer J., Vestergaard M., 2015, *ApJ*, **810**, 86
- Cardelli J. A., Clayton G. C., Mathis J. S., 1989, *ApJ*, **345**, 245
- Chabrier G., 2003, *PASP*, **115**, 763
- Chang K., Refsdal S., 1984, *A&A*, **132**, 168
- Collinson J., 2016, *MNRAS*, submitted
- Drake A. J., et al., 2009, *ApJ*, **696**, 870
- Edelson R., et al., 2015, *ApJ*, **806**, 129
- Eigenbrod A., Courbin F., Sluse D., Meylan G., Agol E., 2008, *A&A*, **480**, 647
- Elvis M., et al., 1994, *ApJS*, **95**, 1
- Foreman-Mackey D., Hogg D. W., Lang D., Goodman J., 2013, *PASP*, **125**, 306
- Gardner E., Done C., 2016, preprint, ([arXiv:1603.09564](https://arxiv.org/abs/1603.09564))
- Hawkins M. R. S., 2002, *MNRAS*, **329**, 76
- Irwin M. J., Webster R. L., Hewett P. C., Corrigan R. T., Jedrzejewski R. I., 1989, *AJ*, **98**, 1989
- Jiménez-Vicente J., 2016, *Astrophysical Applications of Gravitational Lensing*. Cambridge University Press (in press)
- Jiménez-Vicente J., Mediavilla E., Muñoz J. A., Kochanek C. S., 2012, *ApJ*, **751**, 106
- Jiménez-Vicente J., Mediavilla E., Kochanek C. S., Muñoz J. A., Motta V., Falco E., Mosquera A. M., 2014, *ApJ*, **783**, 47
- Kaspi S., Brandt W. N., Maoz D., Netzer H., Schneider D. P., Shemmer O., 2007, *ApJ*, **659**, 997
- Kelly B. C., Bechtold J., Siemiginowska A., 2009, *ApJ*, **698**, 895
- Kelly B. C., Sobolewska M., Siemiginowska A., 2011, *ApJ*, **730**, 52
- Kozłowski S., 2016, *MNRAS*, **459**, 2787
- Lawrence A., 2012, *MNRAS*, **423**, 451
- Lawrence A., et al., 2016, preprint, ([arXiv:1605.07842](https://arxiv.org/abs/1605.07842))
- MacLeod C. L., et al., 2010, *ApJ*, **721**, 1014
- MacLeod C. L., et al., 2012, *ApJ*, **753**, 106
- MacLeod C. L., et al., 2015, *ApJ*, **806**, 258
- MacLeod C. L., et al., 2016, *MNRAS*, **457**, 389
- Magnier E. A., et al., 2013, *ApJS*, **205**, 20
- McLure R. J., Dunlop J. S., 2004, *MNRAS*, **352**, 1390
- Metzroth K. G., Onken C. A., Peterson B. M., 2006, *ApJ*, **647**, 901
- Morgan C. W., Kochanek C. S., Morgan N. D., Falco E. E., 2010, *ApJ*, **712**, 1129
- Mortonson M. J., Schechter P. L., Wambsganss J., 2005, *ApJ*, **628**, 594
- Mosquera A. M., Kochanek C. S., 2011, *ApJ*, **738**, 96
- Onken C. A., Peterson B. M., 2002, *ApJ*, **572**, 746
- Peterson B. M., Wandel A., 1999, *ApJ*, **521**, L95
- Peterson B. M., et al., 2013, *ApJ*, **779**, 109
- Planck Collaboration et al., 2014, *A&A*, **571**, A16
- Schlafly E. F., Finkbeiner D. P., 2011, *ApJ*, **737**, 103
- Schlafly E. F., et al., 2012, *ApJ*, **756**, 158
- Shappee B. J., et al., 2014, *ApJ*, **788**, 48
- Shen Y., et al., 2016, *ApJ*, **818**, 30
- Sluse D., et al., 2011, *A&A*, **528**, A100
- Sluse D., Hutsemékers D., Courbin F., Meylan G., Wambsganss J., 2012, *A&A*, **544**, A62
- Sluse D., Hutsemékers D., Anguita T., Braibant L., Riaud P., 2015, *A&A*, **582**, A109
- Steele I. A., et al., 2004, in Oschmann Jr. J. M., ed., *Proc. SPIE Vol. 5489, Ground-based Telescopes*. pp 679–692, doi:10.1117/12.551456
- Sun M., et al., 2015, *ApJ*, **811**, 42
- Tonry J. L., et al., 2012, *ApJ*, **750**, 99
- Trevese D., Perna M., Vagnetti F., Saturni F. G., Dadina M., 2014, *ApJ*, **795**, 164
- Vernardos G., Fluke C. J., Bate N. F., Croton D., Vohl D., 2015, *ApJS*, **217**, 23
- Véron-Cetty M.-P., Joly M., Véron P., 2004, *A&A*, **417**, 515
- Vestergaard M., Wilkes B. J., 2001, *ApJS*, **134**, 1
- Wambsganss J., 2006, in Meylan G., Jetzer P., North P., Schneider P., Kochanek C. S., Wambsganss J., eds, *Saas-Fee Advanced Course 33: Gravitational Lensing: Strong, Weak and Micro*. pp 453–540
- York D. G., et al., 2006, *MNRAS*, **367**, 945
- van Dokkum P. G., 2001, *PASP*, **113**, 1420

APPENDIX A: APPENDIX

This paper has been typeset from a $\text{\TeX}/\text{\LaTeX}$ file prepared by the author.

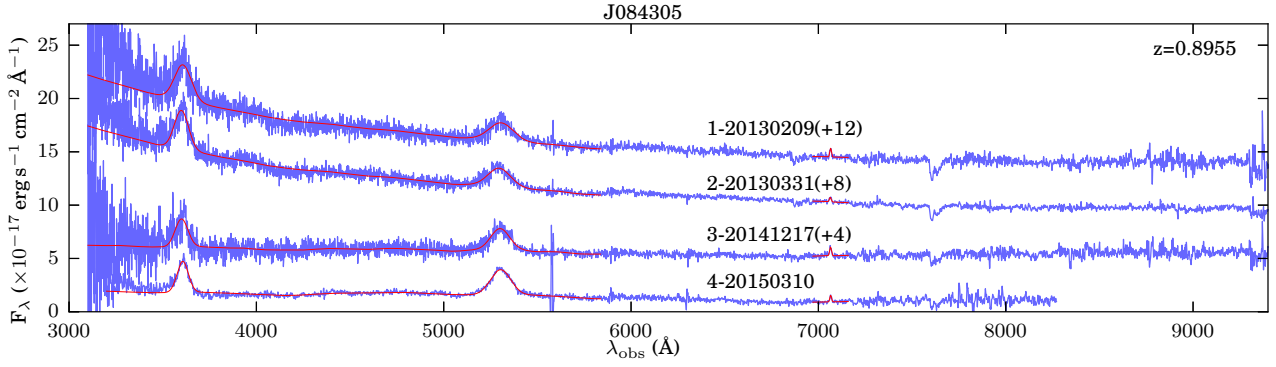


Figure A1. Spectra for J084305 as produced by our reduction pipeline. They have been scaled to our microlensing model (5.1) and are corrected for Milky Way reddening. The red lines show the best-fit models from the fitting process.

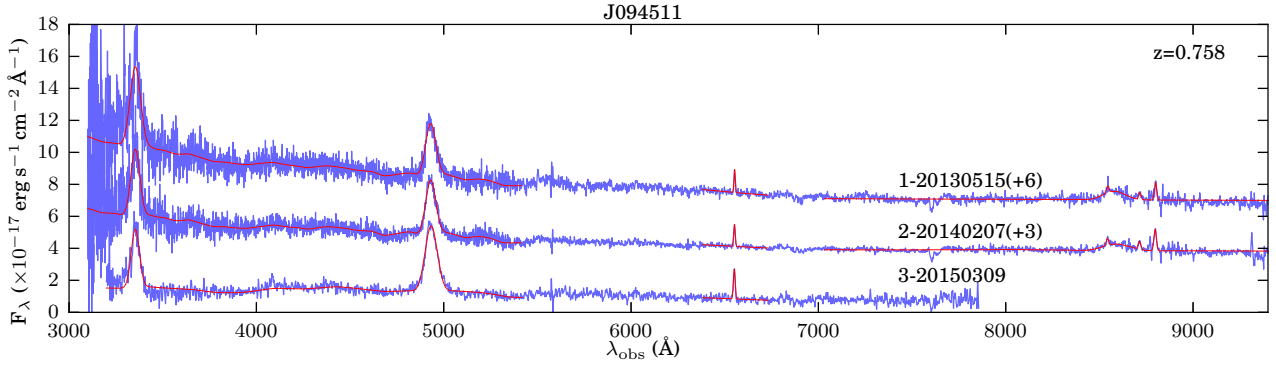


Figure A2. Spectra for J094511 as produced by our reduction pipeline. They have been scaled to our microlensing model (5.1) and are corrected for Milky Way reddening. The red lines show the best-fit models from the fitting process.

Table A1. Data table. (1) Scaling correction factor applied to the spectrum as described in 2.3.3. (2) Power law slope from the fit given by Eq. 1. (3) Observed AGN monochromatic continuum flux at rest-frame 3000Å calculated from the power-law fit to the UV region. (4) AGN monochromatic continuum luminosity derived from (2). (5/6/7) Line centre, sigma and total line flux from the gaussian fit to MgII in the observed frame. For J103837 the values are from the narrower of the two broad MgII components. (8) Black hole mass calculated using the McLure & Dunlop (2004) relation. Errors are from the fitting process only.

target	MJD	scale	β	f_{3000} erg s ⁻¹ cm ⁻² Å ⁻¹ ×10 ⁻¹⁷ (3)	L ₃₀₀₀ log ₁₀ (erg s ⁻¹) (4)	λ_{MgII} Å (5)	σ_{MgII} Å (6)	A_{MgII} erg s ⁻¹ cm ⁻² ×10 ⁻¹⁵ (7)	M_{BH} log ₁₀ (M _⊙) (8)
		(1)	(2)						
J084305-1	56333.2	1.04	-1.82±0.02	3.378±0.026	44.907±0.002	5304.9±2.2	63.0±2.3	2.84±0.09	8.91±0.03
J084305-2	56382.9	0.83	-1.86±0.01	3.035±0.018	44.861±0.002	5294.4±1.7	59.2±1.7	2.83±0.07	8.83±0.02
J084305-3	57009.0	1.25	-0.78±0.04	1.368±0.024	44.515±0.005	5299.5±1.5	51.0±1.5	2.91±0.07	8.49±0.02
J084305-4	57092.2	1.42	-0.82±0.05	1.099±0.029	44.420±0.008	5303.5±0.9	54.8±0.9	3.36±0.05	8.49±0.01
J094511-1	56427.9	0.91	-1.75±0.04	1.899±0.036	44.446±0.006	4930.3±0.6	28.5±0.6	2.60±0.05	8.00±0.02
J094511-2	56695.9	0.80	-1.75±0.03	1.308±0.023	44.284±0.005	4930.3±0.4	27.9±0.4	2.64±0.03	7.89±0.01
J094511-3	57091.2	1.28	-0.99±0.07	0.848±0.034	44.096±0.012	4932.9±0.4	32.9±0.4	3.50±0.04	7.91±0.01
J142232-1	56335.2	1.04	-1.90±0.01	3.008±0.017	45.093±0.002	5813.2±0.9	40.3±0.9	1.78±0.03	8.56±0.02
J142232-2	56428.1	1.17	-1.91±0.02	2.664±0.028	45.040±0.003	5825.9±1.9	55.1±2.2	1.93±0.06	8.80±0.03
J142232-3	56511.9	1.02	-1.99±0.02	2.238±0.018	44.964±0.002	5820.3±1.3	44.8±1.3	1.69±0.04	8.57±0.02
J142232-4	56696.2	0.80	-1.13±0.01	1.892±0.011	44.891±0.002	5807.5±0.7	49.3±0.8	2.02±0.02	8.61±0.01
J142232-5	56862.9	0.89	-1.43±0.02	1.116±0.010	44.662±0.003	5810.9±0.7	46.3±0.8	1.37±0.02	8.42±0.01
J142232-7	57136.1	0.77	-1.32±0.02	1.061±0.012	44.640±0.003	5808.5±1.1	48.5±1.2	1.25±0.02	8.44±0.02
J103837-1	56335.1	1.42	-1.92±0.03	6.016±0.095	44.699±0.005	4533.6±0.8	20.3±1.4	3.00±0.52	7.94±0.06
J103837-2	56427.9	1.01	-1.24±0.06	2.515±0.073	44.320±0.008	4534.8±0.7	18.2±1.5	2.37±0.55	7.61±0.07
J103837-3	57133.9	0.96	-1.38±0.01	5.227±0.037	44.638±0.002	4537.4±0.5	18.3±0.9	2.01±0.29	7.81±0.04

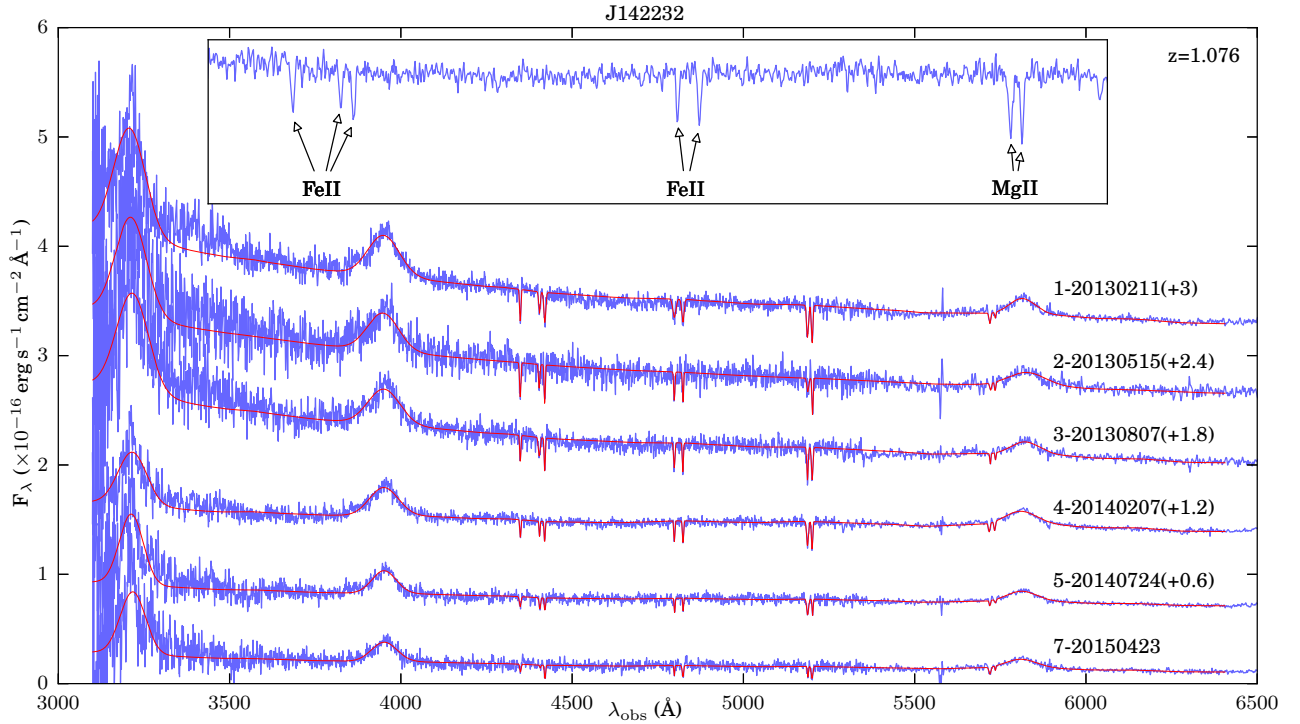


Figure A3. Spectra for J142232 as produced by our reduction pipeline. They have been scaled to our LT data (2.3.3) and are corrected for Milky Way reddening. The red lines show the best-fit models from the fitting process. Inset is a zoomed region of the central portion of the 4th epoch to highlight the absorption complex.

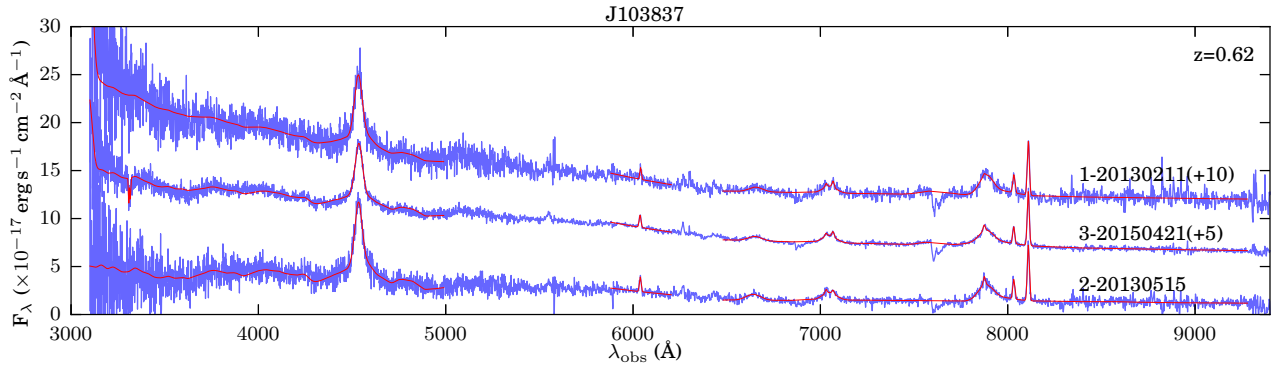


Figure A4. Spectra for J103837 as produced by our reduction pipeline. They have been scaled to our LT data (2.3.3) and are corrected for Milky Way reddening. The red lines show the best-fit models from the fitting process. Inset is a zoomed region of the central portion of the 4th epoch to highlight the absorption complex.

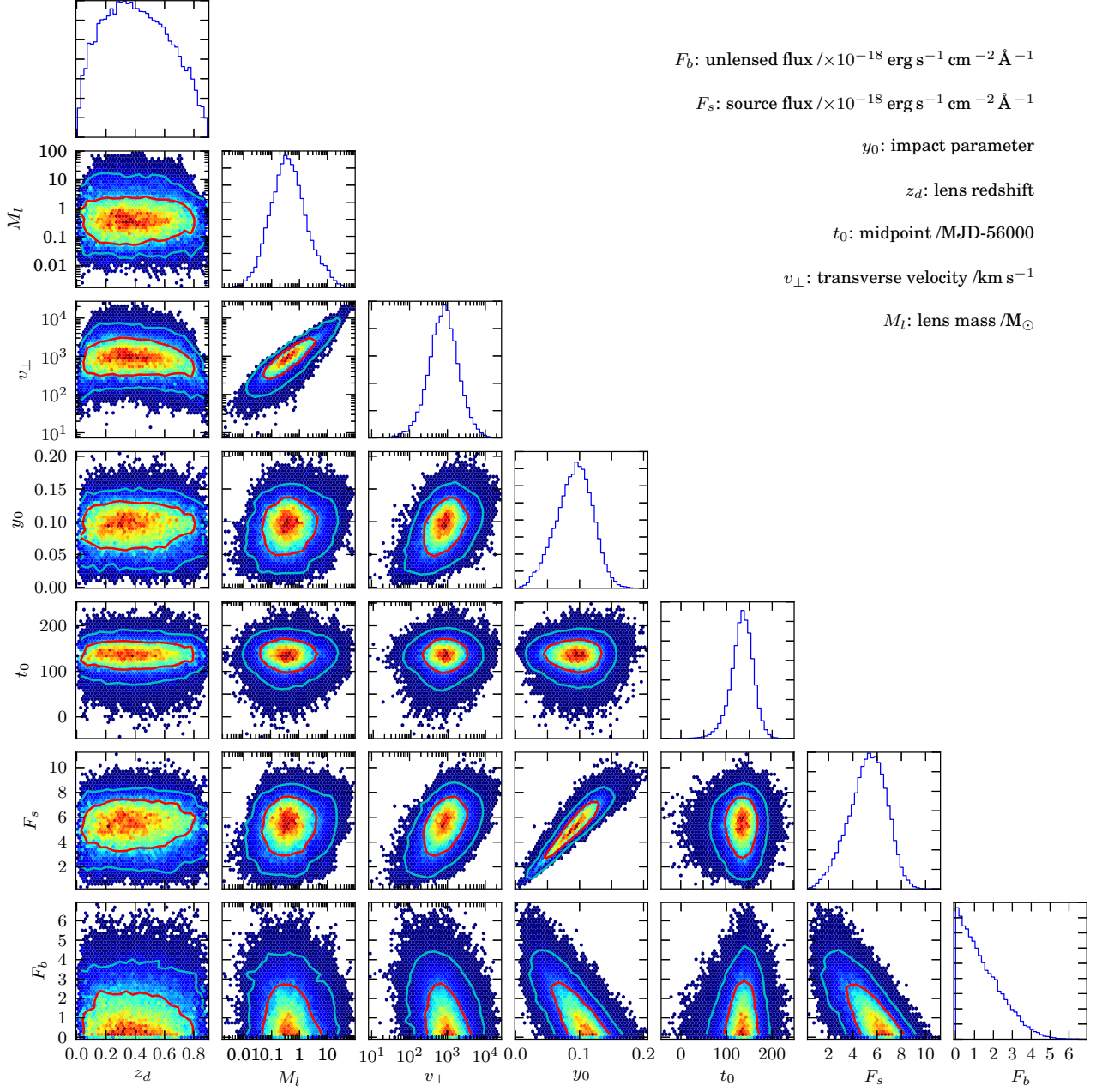


Figure A5. Corner plot from the MCMC analysis showing the one- and two-dimensional posterior probability distributions for J084305.

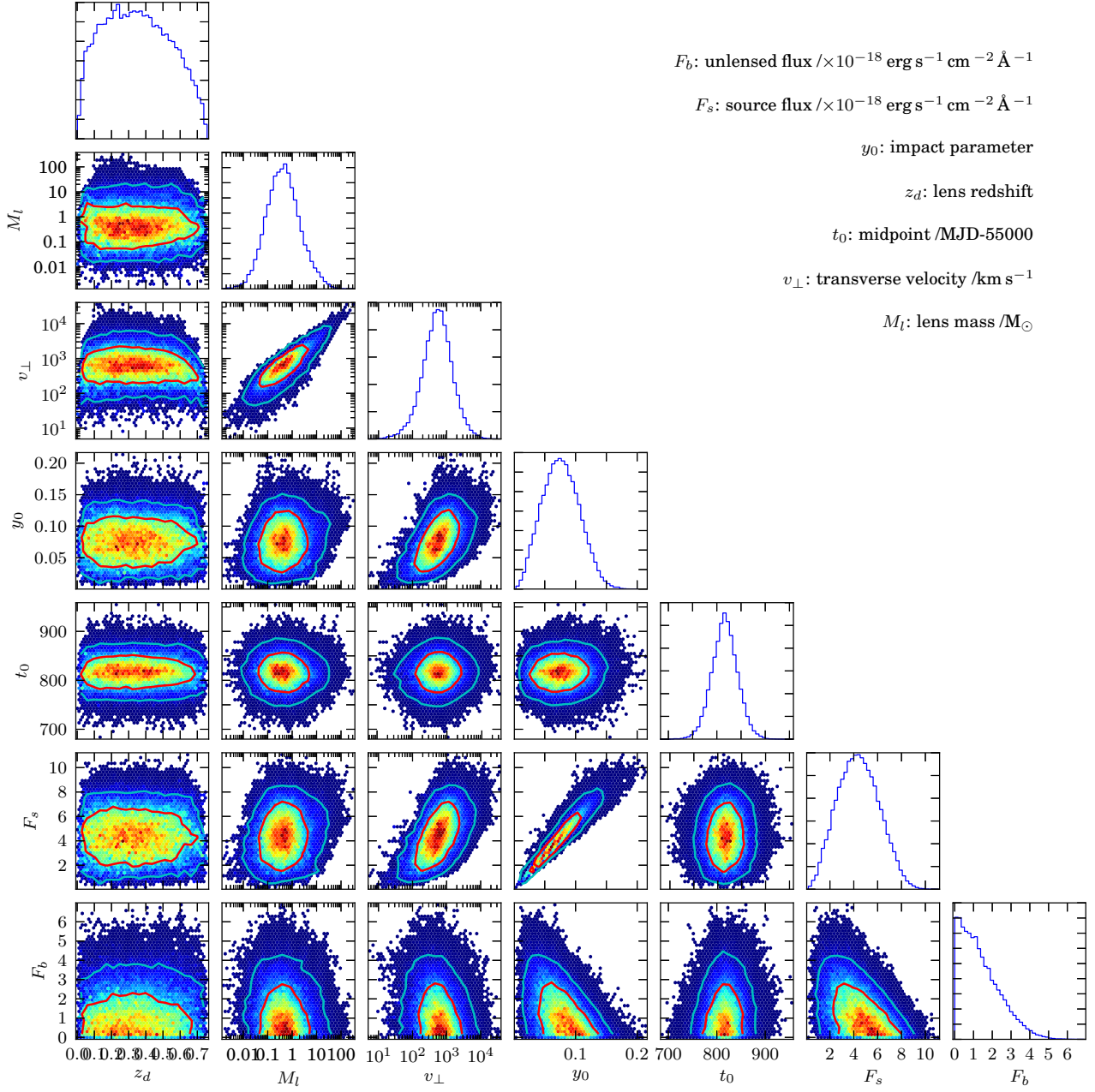


Figure A6. Corner plot from the MCMC analysis showing the one- and two-dimensional posterior probability distributions for J094511.